Journal of the Meteorological Society of Japan

EARLY ONLINE RELEASE

The DOI for this manuscript is
DOI:10.2151/jmsj.2022-019
J-STAGE Advance published date: December 14th, 2021

Interactions between a tropical cyclone and upper-tropospheric cold-core lows simulated by an atmosphere-wave-ocean coupled model: A case study of Typhoon Jongdari (2018)

Akiyoshi WADA*, Wataru YANASE, Kozo OKAMOTO

Department of Typhoon and Severe Weather Research
Meteorological Research Institute, Tsukuba, Japan

December 05, 2021

---

* Corresponding author: Akiyoshi Wada, Meteorological Research Institute, 1-1, Nagamine, Tsukuba, Ibaraki 305-0052, Japan.
Email: awada@mri-jma.go.jp
Tel: +81-29-853-8574
Fax: +81-29-853-8735

Abstract

Typhoon Jongdari (2018) took an unusual track along the circumference of an upper-tropospheric cold low (UTCL) before making landfall in Japan on 29 July. To investigate the effects of atmosphere-ocean interactions and interactions between the UTCL and Jongdari on the storm's track, numerical simulations were conducted with a 3-km-mesh nonhydrostatic atmosphere model and an atmosphere-wave-ocean coupled model, using different initial conditions created by adopting different initial times. The UTCL was characterized by high potential vorticity (PV), low pressure, and low relative humidity on the 355 K isotherm. While the UTCL moved southwestward north of Jongdari from 25 to 27 July, simulation results indicate that Jongdari traveled counterclockwise along the circumference of the UTCL. After Jongdari began moving westward, the coupled model simulated sea surface cooling along the track. Jongdari weakened after making landfall while the UTCL also weakened south of Japan. In particular, latent heat flux from the sea and the resulting humidification of the upper troposphere through the convection affected the UTCL. When Jongdari redeveloped over the ocean south of Kyushu, some simulations showed that Jongdari merged with the UTCL there as a result of high PV in Jongdari and relatively low upper-tropospheric PV near the UTCL. Ocean coupling helped sustain the upper-tropospheric PV near the UTCL and weakened the column of elevated PV associated with Jongdari, which affected the location of the tropopause folding

transformed from the UTCL by lowering the PV column of Jongdari and weakening the upper-tropospheric outflow from the center. Because the steering flow of Jongdari was affected by the geostrophic-balanced cyclonic circulation created by the UTCL, a larger difference in the atmospheric initial conditions had a stronger influence on track and intensity simulations of both Jongdari and the UTCL than the effects of ocean coupling.

Keywords Atmosphere-wave-ocean coupled model; Typhoon; Upper-tropospheric cold low; Potential vorticity

1. Introduction

Typhoon Jongdari originated as a tropical depression that was updated to a tropical storm around 19.7°N, 136.7°E at 12 UTC on 24 July 2018, according to best track data from the Regional Specialized Meteorological Center Tokyo (https://www.jma.go.jp/jma/jma-eng/jma-center/rsmc-hp-pub-eg/besttrack.html, accessed October 16, 2021). It then followed an unusual course. After moving northward in the early intensification phase from 12 UTC on 24 to 06 UTC on 25 July, Jongdari moved cyclonically in a wide arc corresponding to a circle of approximately 600 km radius, reaching a central pressure of 960 hPa at 00 UTC on 27 July (Figs. 1a–c). Jongdari made landfall in Shima City, Mie Prefecture (the asterisk in Fig. 1c) at 15 UTC on 28 July and moved over the Japanese archipelago (Fig. 1d). It entered the East China Sea at 21 UTC on 29 July and moved cyclonically in a circular loop approximately 150 km in radius over the ocean south of Kyushu until 31 July (Figs. 1e, f); it then moved westward over the East China Sea. Elucidating the mechanism of Jongdari's irregular and unusual track is a scientifically interesting topic.

During its early intensification phase, Jongdari had to its north a cold vortex in the upper troposphere over the ocean east of Japan and west of Typhoon Wukong (2018) (Fig. 1a). The cold vortex was an upper-tropospheric cold low (UTCL) or upper-tropospheric cyclonic low, a low-pressure system that has become completely detached from the basic westerly current in the jet stream (Nieto et al. 2005, 2008). These form more often in summer than in winter (Wei et al. 2016), are usually advected slowly toward the equatorial side of

80 the mid-latitude westerlies, and often stay over the same region for several days (Gimeno
81 et al. 2007). Their four-stage life cycle is divided into upper-level trough, tear-off, cut-off, and
82 final stages. At the time Jongdari was intensifying on 25 July, the cold vortex was already
83 cut off from the mid-latitude westerlies. From 25 to 28 July, the UTCL was in the cut-off stage
84 and moved slowly southwestward while weakening. As Jongdari approached Japan, it
85 moved cyclonically along the circumference of this UTCL.

86 Previous studies have suggested that UTCLs originate in a tropical upper-
87 tropospheric trough (TUTT) and lead directly to the formation and development of tropical
88 cyclones (TCs) because of the presence of the cold air mass aloft or by acting as additional
89 outflow channels to reinforce TC development (Sadler 1976, 1978). The outflow channels
90 are connected to large-scale westerlies through the enhancement of upper-level divergence,
91 which creates favorable conditions for interactions of upper-level troughs with TCs (Sadler
92 1976). An investigation of the relationship between TCs and UTCLs in the western North
93 Pacific from 2000 to 2012 by Wei et al. (2016) found that 83% of UTCLs were part of a TUTT
94 and the rest were cut off from westerlies; it also reported that 73% of TCs coexisted with a
95 UTCL and 44% of TCs interacted with a UTCL, whereas only 21% of UTCLs coexisting with
96 TCs were within an initial cutoff distance of 15° of each other.

97 Wei et al. (2016) also showed that UTCLs can affect the track of TCs, depending on
98 their relative distance and orientation. TCs in the southern half of a UTCL are more likely to
99 intensify and those in the northern half are more likely to weaken, and TCs in a UTCL's

northeastern quadrant tend to weaken more slowly than those in the western North Pacific climatology. Patla et al. (2009) proposed a graphical representation of the conceptual model of the influence of a TUTT cell or UTCL on TC motions as a guidance for operational use at the Joint Typhoon Warning Center. Yan et al. (2021) reported that the removal of the observed UTCL from their numerical simulations of Jongdari substantially changed the simulated motion and intensity of Jongdari.

In addition to the statistical studies, dynamics between a UTCL and a TC have ever been studied. Molinari et al. (1998) noted that the dynamics between a UTCL and a TC are affected by three advective transports related to vertical wind shear, diabatic heating, and vortex interaction: the advection of the upper-tropospheric low potential vorticity (PV) anomaly away from the TC in the direction of the vertical wind shear vector (Shapiro 1992; Wu and Emanuel 1993), the mutual advection between the positive and negative PV anomalies at 350 K, and the mutual advection between 350 K anomalies and anomalies above and below them (Jones 1995). These dynamics, however, do not include the effect of multi-scale interactions such as the interactions between the two vortices and mid-latitude westerlies and between the atmosphere and the ocean. In that sense, the understanding on the dynamics of the interactions between a UTCL and a TC is still not complete. Numerical simulation by a sophisticated atmosphere-wave-ocean coupled model (Wada et al. 2010, 2018) is one of the effective methods for studying the multi-scale interactions. The dynamics of vortex interactions as well as the behavior of a UTCL moving toward low latitudes should

120 be clarified in the coupled atmosphere-ocean model framework to better understand the role
121 of the UTCL in Jongdari's unusual track and to improve the accuracy of track predictions.

122 This study sought to understand the mechanism by which the UTCL influenced
123 Jongdari's track and intensity evolution and to understand the role of atmosphere-ocean
124 interactions and initial conditions in that mechanism. For those purposes, we conducted
125 numerical simulations with a 3-km-mesh nonhydrostatic atmosphere model (NHM) and an
126 atmosphere-wave-ocean coupled model (CPL), using different atmospheric and oceanic
127 initial conditions generated by adopting different initial times.

128 The following sections are as follows. Section 2 explains the experimental design of
129 our numerical simulations. Section 3 consists of five subsections and describes the results
130 simulated by the NHM and CPL with different initial times. Section 4 presents a discussion
131 and summary.

132 **2. Experimental design**

133 *2.1 Data*

134 Our simulations by the NHM and CPL required initial conditions for the atmosphere
135 and ocean and boundary conditions for the atmosphere; the ocean surface wave model
136 included in the CPL assumed a motionless initial condition.

137 The atmospheric initial and boundary conditions were generated from Japan
138 Meteorological Agency (JMA) 6-hourly global atmospheric analysis data with a horizontal
139 grid spacing of approximately 20 km. The initial times ranged from 12 UTC on 25 July to 12

UTC on 28 July 2018 at 6 h intervals. The atmospheric boundary condition at each initial time was generated every 6 h during the integration time. The oceanic initial condition, other than sea surface temperature (SST), was generated from the JMA daily North Pacific oceanic analysis data, which include water temperature, salinity, currents, and sea surface height anomaly data at a horizontal resolution of 0.5° in longitude and latitude. The oceanic initial condition was created at 6 h intervals from 12 UTC on 25 July to 12 UTC on 28 July 2018, depending on the initial integration day because the oceanic analysis data is a daily product, and the same data is imposed throughout a day.

The SST initial condition was derived from the Microwave Optimally Interpolated SST daily product (obtained from the Remote Sensing Systems site, http://www.remss.com/ ,accessed October 16, 2021). This is a daily merged satellite dataset that combines measurements by the WindSat (Gaiser et al. 2004), the Advanced Microwave Scanning Radiometers 2, and the Global Precipitation Measurement Microwave Imager. It covers the global ocean with a 0.25° horizontal spacing at a depth of approximately 1 m. We used brightness temperatures from the Himawari-8 infrared imager to monitor the behavior of the UTCL and hourly atmospheric motion vectors above 350 hPa height, derived from the Himawari-8 brightness temperatures, to monitor the upper-tropospheric flow.

2.2 Models

The NHM and CPL used in this study have been used in many studies to analyze the role of atmosphere-ocean interactions on TC simulations (e.g., Wada et al. 2018; Wada and

160 Oyama 2018; Oyama and Wada 2019; Wada 2021). The NHM was introduced in Saito
161 (2012). The components of the coupled model (Wada et al. 2010) include the Meteorological
162 Research Institute (MRI) third-generation ocean surface-wave model MRI-III (Japan
163 Meteorological Agency 2013) and a multilayer ocean model developed by MRI based on
164 Bender et al. (1993). The ocean model includes a diurnally varying SST scheme based on
165 Schiller and Godfrey (2005) with the short-wave absorption/penetration formulation of
166 Ohlmann and Siegel (2000). Details of the MRI models and the exchange processes
167 between the atmosphere, ocean surface waves, and ocean are described in Wada et al.
168 (2018).

169 The physical processes in our models are important for determining the accuracy of
170 simulation results. We relied on an explicit three-ice bulk microphysics scheme (Ikawa and
171 Saito 1991; Lin et al. 1983). Air-sea momentum fluxes and sensible and latent heat fluxes,
172 with exchange coefficients for air-sea momentum and enthalpy transfers over the sea, were
173 based either on bulk formulas (Kondo 1975) or, when the ocean-wave model was coupled
174 (Wada et al. 2010), on the roughness lengths proposed by Taylor and Yelland (2001), a sea
175 spray formulation (Wada et al. 2018), a turbulent closure model (Klemp and Wilhelmson
176 1978; Deardorff 1980), and a radiation scheme (Sugi et al. 1990). These are also the same
177 as those specified in Wada et al. (2018) and Wada (2021).

178 *2.3 Configuration of numerical simulations*

179 The horizontal resolution of NHM and CPL was 3 km. The computational domain was

single and approximately 2760 km × 2760 km, centered at 30°N, 140°E. All simulations used 55 levels in vertical coordinates, with intervals ranging from 40 m for the near-surface layer to 1013 m for the uppermost layer. The top height was approximately 27 km. The lowermost end index for upper Rayleigh damping layer was 44 (approximately 17.5km). The width of lateral boundary relaxation sponge layers was 150 km in all experiment. The time steps were 6 s for NHM, 36 s for the ocean model, and 6 min for MRI-III. The physical components were exchanged between NHM and the ocean model every 36 s and between those models and MRI-III every 6 min. The integration time was 144 h in all experiments. Simulations by each model incorporated 13 initial conditions at 6 h intervals, for a total of 26 simulations. It should be noted that the difference of the width of lateral boundary relaxation sponge layers could affect track and intensity of simulated Jongdari so that the simulation results were validated with RSMC best track data.

3 Results

3.1 Behavior of Jongdari and the UTCL

The passage of Jongdari during its intensification phase induced sea surface cooling on the right side (outside) along its counterclockwise track (Fig. 2). This cooling is known as the negative feedback effect on TCs and helped suppress the intensification of Jongdari (e.g., Bender et al. 1993; Wada et al. 2018). However, SST was relatively high at 28–29°C from 25 to 28 July over the ocean south of Kyushu, where Jongdari passed after 21 UTC on 29 July. The warm surface water south of Kyushu was a favorable condition for Jongdari's

200 second intensification (Kuo et al. 2018; Wu et al. 2008).

201 The brightness temperature and atmospheric motion vectors clearly show the dry
202 area around the UTCL and the clockwise flow circulation centered on the continental high at
203 12 UTC on 25 July (Fig. 3). Northeasterly winds were relatively strong southwest of the
204 UTCL at that time (C in Fig. 3). While the UTCL moved southwestward, Jongdari,
205 represented by a cluster of low brightness temperature areas, moved cyclonically along its
206 circumference. As Jongdari approached the UTCL after making landfall in Japan, the dry
207 area in the UTCL gradually became subdued, an indication that the UTCL was weakening.
208 After Jongdari moved over the ocean south of Kyushu, the TC appeared to occupy the same
209 position as the UTCL. Our simulations of the interactions between the UTCL and Jongdari
210 sought to investigate the role of Jongdari, a marginal TC (Molinari et al. 1998), in the UTCL
211 transition and vice versa.

212 *3.2 Simulated track and central pressure*

213 Numerical simulations of TCs are strongly affected by the uncertainty of the initial
214 conditions (e.g., Wada and Kunii 2017; Wang and Wu 2004). Even if a simulation at a given
215 initial condition fits the observations and the best track analysis of a TC, it does not mean
216 that the numerical system used can repeat that success with another initial condition at
217 another initial time. We therefore used ensemble simulation results by the NHM and CPL to
218 obtain more accurate simulated Jongdari's irregular track without affecting the uncertainty
219 included in the atmospheric initial conditions.

Our two sets of 13 simulations successfully tracked the center position and central pressure of the simulated Jongdari from each initial time and in each model used. The simulated center position of Jongdari was determined as the grid point with the lowest pressure at sea level. The center of the simulated UTCL was the grid point with the lowest pressure at 12000 m altitude, consistent with previous studies (e.g., Wei et al. 2016). Both positions were tracked from 12 UTC on 25 July to 00 UTC on 2 August.

Regarding the predictability of Jongdari's track, the error tendencies in predictions carried out by major numerical prediction centers such as the European Centre for Medium-Range Weather Forecasts (ECMWF), the Meteorological Service of Canada and Deutsche Wetterdienst showed westward deflection in the first intensification phase and northward deflection in the mature, landfalling, and weakening phases when the initial time of the prediction was 12 UTC on 25 July (not shown). The ECMWF ensemble forecasts showed a westward shift in the track, whereas those of the National Centers for Environmental Prediction showed an eastward shift (Lei et al. 2020). One factor in this difference in track forecasts is the poor simulation of intensity due to the model's coarse horizontal resolution (Fierro et al. 2009; Kanada and Wada 2016).

Figures 4a, b show the tracks of Jongdari and the UTCL simulated by the NHM (hereafter, the noncoupled-model simulation) (Fig. 4a) and by the CPL (hereafter, the coupled-model simulation) (Fig. 4b). Both of these simulations reduced the northward deflection in the mature, landfalling, and weakening phases to some extent compared with

240 the previously mentioned track forecasts, but they did not reduce the westward deflection in
241 the intensification phase. In addition, all simulations failed to reproduce the looping feature
242 south of Kyushu. The smaller loop in the simulations was different from the larger loop of
243 the best track analysis. The simulated UTCL first appeared east of Japan around 35°N,
244 148°E, moved southwestward over the ocean, and then stayed around 30°N, 136°E, which
245 is consistent with the observed behavior of the UTCL shown in Fig. 3. Figures 4c, d show
246 the positions of simulated UTCL relative to the simulated TC positions in the noncoupled-
247 (Fig. 4c) and coupled-model simulation (Fig. 4d). The simulated UTCL approached the TC
248 center counterclockwise from 12 UTC on 25 July to 00 UTC on 29 July and then stayed on
249 the east side of TC center. The noncoupled- and coupled-model simulations had no notable
250 difference in their TC tracks, which suggests that the sea surface cooling induced by
251 Jongdari had little or no effect on the track simulations. This result is consistent with previous
252 studies (Bender et al. 1993; Ito et al. 2015; Mogensen et al. 2017; Wada et al. 2018). In
253 addition, the sea surface cooling induced by Jongdari had little or no effect on the relative
254 position of the simulated UTCL to the simulated TC. In other words, the difference in the
255 simulated TC track and movement of the UTCL was mainly caused by the difference in the
256 initial conditions.

257 Figure 5a shows the time series of the best track central pressure and mean central
258 pressures averaged among 13 simulations in the noncoupled- and coupled-model
259 simulations with central pressures at five different initial times (12 UTC 25, 09 UTC 27, 12

UTC 27, 18 UTC 27 and 00 UTC 28 July). These show underdevelopment from 12 UTC 25 July to 00 UTC 29 July and then overdevelopment after 00 UTC 29 July. At the time when the real Jongdari was over land at 16 UTC 28 July, the simulated Jongdari was moving over the ocean to the south of the best track, which was favorable for the development of Jongdari. The ocean coupling effect tended to alleviate the overdevelopment of the simulated Jongdari due to sea surface cooling (Bender et al. 1993; Ito et al. 2015; Mogensen et al. 2017; Wada et al. 2018; Wada 2021). Figure 5b shows the time series of mean radius of maximum wind speed at 20-m altitude averaged among 13 simulations in the noncoupled- and coupled-model simulations, respectively. The range of the evolution of the radius of maximum winds varied from 30 to 80 km from 00 UTC on 26 July to 12 UTC on 31 July, an indication that the size of simulated TC was relatively small compared with the distance between the TC and the UTCL (Figs. 4c, d). When the difference in the average radius of maximum winds between the noncoupled- and coupled-model simulations was tested, no significant difference was found at the 95% confidence level based on t-test. Therefore, the effect of ocean coupling on the simulated TC size is not significant in the present study.

Table 1 lists the simulation results (position, central pressure, and maximum wind speed at 20 m), the best track data for 144 h for each initial time and their averages. The average position from the coupled-model simulations (30.13°N, 133.00°E) was southeast of the average position from the noncoupled-model simulations (30.24°N, 132.97°E) and slightly closer to the average position obtained from the best track data (30.65°N,

135.37°E). The same was true for the average central pressures: 978.52 hPa from the coupled-model simulations, 973.90 hPa from the noncoupled-model simulations, and 980.19 hPa from the best track data. The average maximum wind speed was 28.47 m s^{-1} in the coupled-model simulations, which was weaker than the noncoupled-model results (33.74 m s^{-1}) and closer to the best track result (25.54 m s^{-1}). These results suggest that the use of CPL slightly improved the track and intensity predictions for Jongdari. However, the prediction error due to the difference in initial times was much greater than the effect of ocean coupling (Table 1).

Figure 6 shows the time series of the average differences in the track and central pressure between the noncoupled- and coupled-model simulations. The CPL reduced the error in the track simulations after 60 h compared with the NHM. The intensity prediction was closer to the best track for the noncoupled-model simulations up to 60 h and for the coupled-model simulations after 84 h. The improvement in central pressure simulations in the latter part of the integration time is an expectable effect of ocean coupling (Bender et al. 1993; Ito et al. 2015; Mogensen et al. 2017; Wada et al. 2010, 2018; Wada 2021). The question is how ocean coupling affected the TC vortex itself and the UTCL surrounding the TC. The next section discusses how Jongdari and the UTCL behaved in the simulation results.

3.3 Interaction of simulated Jongdari with the UTCL

This section presents Jongdari and the UTCL in the noncoupled-model simulations.

300 Figure 7 maps pressure at approximately 10 km altitude along with sea-level pressure and
301 Ertel's PV (Davis and Emanuel 1991) (1 PV unit = 10^{-6} m^2 s^{-1} K kg^{-1}) on the 355 K isotherm
302 and shows vertical profiles of PV, potential temperature and horizontal-vertical wind vectors
303 parallel to the cross section along the line connecting the centers of Jongdari and the UTCL
304 at the integration times of 0, 36, 72, and 108 h after the initial time of 12 UTC on 25 July. It
305 should be noted that the height of 10 km is lower than that of the UTCL (12 km) used in Figs.
306 3 and 4, although this difference does not affect our conclusions. The horizontal distributions
307 in all cases in this paper are averaged over the neighboring 16 grid cells (approximately 50
308 km) except the distribution of hourly precipitation.

309 In the intensification phase (0–36 h), the TC vortex was relatively small (Figs. 7a, b),
310 resembling that of a marginal tropical storm (Molinari et al. 1998) or a midget TC (Lander
311 1994). However, a tower of positive PV (>1 PV unit) associated with the TC (hereafter
312 referred to as the PV tower) was clearly depicted extending from the lower to the middle
313 troposphere (Fig. 7c). On the other hand, the UTCL was characterized by low pressure
314 around 10000 m and high PV in the upper troposphere (Fig. 7b). As Jongdari moved north-
315 northeastward in the simulation and the UTCL moved southwestward (Figs. 7d, e), southerly
316 winds around the eastern edge of the UTCL strengthened. The simulated TC moved along
317 the northeastern edge of the cyclonic circulation, and the value of PV on the 355 K isotherm
318 became small. Jongdari was intensifying in the simulation when the outflow from the PV
319 tower became evident (Fig. 7f).

As the simulated Jongdari moved westward along the Japanese coast (Fig. 7g) and the high-PV area in the UTCL descended in altitude while the UTCL was moving southwestward (Fig. 7h), the PV tower approached the Japanese archipelago (Fig. 7i) and then weakened (Fig. 7l). The high-PV area on the 355 K isotherm was stretching and cyclonically folding (Fig. 7h), resembling the deformation of a fluid surface computed by a barotropic model in which the layers behave like a two-dimensional ideal fluid (Welander 1955). In the simulation, Jongdari continued to follow the geostrophic-balanced cyclonic circulation centered at the UTCL, which is one of the factors that affects the steering flow. When Jongdari moved over the Japanese archipelago, the central pressure in the UTCL increased. This indicates that the TC weakened at that time as a result of surface friction on land. Indeed, the PV tower weakened during the passage over land (not shown). When Jongdari moved over the ocean south of Kyushu in the simulation (Fig. 7j), the cyclonic circulation centered at the area within the UTCL shrank in size (Fig. 7k) and the PV tower intensified again. Even though the UTCL became weak, for convenience we continue to refer to it as the UTCL. At 00 UTC on 30 July in the simulation, the tilt of the upper-level high PV (> 1 PV unit) (Agusti-Panareda et al. 2004) or tropopause folding (Price and Vaughan 1993; Bosart 2003) had reversed from its direction at 36 and 72 h (Fig. 7l), and the location of the TC appeared to be identical to that of the UTCL.

Geostrophic-balanced cyclonic circulation was induced below the UTCL at the initial time (Fig. 8a). As the UTCL moved southwestward at 36 h, the distance between the TC

and the UTCL became closer than before, but the geostrophic circulation of Jongdari was still separated from the geostrophic-balanced cyclonic circulation centered within the UTCL (Fig. 8b). The geostrophic flows within the inner core of Jongdari were clearly found in the intensification phase although in general gradient winds are superior to geostrophic winds within the inner core of a TC (e.g., Miyamoto et al. 2014). At 72 h, geostrophic-balanced cyclonic circulation centered within the UTCL was located in the area centered around 29°N, 136°E (Fig. 8c). The TC moved westward along the northern edge of the UTCL-induced geostrophic-balanced cyclonic circulation. At 108h, the geostrophic-balanced cyclonic circulation was not clear and became part of the inner-core structure of Jongdari (Fig. 8d). This suggests that the magnitude of the UTCL-induced geostrophic-balanced cyclonic circulation became weak. The gradient winds of simulated TC may affect the steering flows. The modification of steering flow due to excessively simulated gradient winds of Jongdari possibly affect the difference in TC tracks between the simulations and best track analysis.

Next, we present the thermodynamic conditions of Jongdari and the UTCL in the simulation. Figure 9 maps the horizontal moisture flux (specific humidity multiplied by momentum per unit mass) at approximately 10 km altitude, the relative humidity at the height of the 355 K isotherm, and the relative humidity along with the potential temperature and horizontal-vertical wind vectors parallel to the cross section along the line between the centers of Jongdari and the UTCL at the integration times of 0, 36, 72, and 108 h after the initial time of 12 UTC on 25 July. Each panel is a counterpart to one in Fig. 7. The reason

360 that the altitude of the horizontal moisture flux and relative humidity is set to 10 km is to
361 clearly show the difference between the dry area at the lower end of UTCL and the
362 convection area of TC.

363 At approximately 10 km altitude, horizontal moisture fluxes were relatively high on the
364 western side of the UTCL, and higher than the moisture fluxes around Jongdari at the initial
365 time, 12 UTC on 25 July (Fig. 9a). This high-moisture area corresponds to the area where
366 relative humidity was higher than 50% on the 355 K isotherm, while relative humidity at the
367 center of the UTCL was close to zero (Fig. 9b). The area of >50% relative humidity was
368 spread zonally around Jongdari. The cross section between Jongdari and the UTCL shows
369 that the tropopause, where the vertical temperature gradient is steeper than that within the
370 troposphere, dropped to approximately 12 km altitude around 36°N, 147°E, while the air with
371 relatively high relative humidity (> 70%) around 8–10 km altitude near 32.5°N, 145°E was
372 carried upward to the upper troposphere (Fig. 9c).

373 At 36 h integration time, the moisture flux was relatively high in the arc-shaped area
374 from north to east of UTCL (Fig. 9d). High moisture fluxes around Jongdari were on the
375 southeastern side of the UTCL and joined the arc-shaped area. The area of low relative
376 humidity (<20%) stretched horizontally to the southwest and then folded around 30°N, 140°E
377 (Fig. 9e). The shape of the arc of dry area was opposite of the arc-shaped area of moisture
378 fluxes. The relative humidity around Jongdari increased on the 355 K isotherm during the
379 intensification phase of TC, and the distance between the UTCL and Jongdari became close

380 (Figs. 4, 9f). The folding of the tropopause around the UTCL was deflected toward Jongdari.
381 Immediately below the area of folding, the relative humidity was locally higher than 70%
382 around 31°N, 139°E, and 8–10 km altitude.

383 At 72 h, the moisture flux was highest around Jongdari just before landfall, and
384 relatively high to the north and northwest of the UTCL. On the 355 K isotherm, an arc of
385 relatively dry air south of Jongdari formed as the dry area of the UTCL combined with another
386 body of dry air, a slot in the middle-to-upper troposphere that flowed cyclonically from the
387 continent (Fig. 9h). The flow of this dry slot was captured by the atmospheric motion vectors
388 above 350 hPa (Fig. 3). The UTCL gained moisture while it was moving southwestward and
389 the distance between the UTCL and Jongdari became closer than before (Figs. 4, 9i). Since
390 TCs simulated by the NHM and CPL are affected by the lateral boundary conditions updated
391 every 6 hours (e.g., Wada, 2017), the influence of the dry slot on the interactions between
392 the UTCL and Jongdari may be affected by the setting of the computational domain and the
393 width of lateral boundary explained in section 2.3. The effect of setting the width of the lateral
394 boundary on the simulation of the dry slot is beyond the scope of this study.

395 At 108 h, high moisture flux was confined to an area around Jongdari (Fig. 9j). On the
396 355 K isotherm, an area of >50% relative humidity likewise surrounded Jongdari (Fig. 9k),
397 and the area of >70% relative humidity around Jongdari had become reduced in altitude
398 from its height at 72 h (Fig. 9l). The UTCL structure was no longer visible in the cross section.
399 During these movements of the UTCL, the dry air within it was gradually humidified and the

400 tropopause around it rose, and it became obscured as it approached and then coalesced
401 with Jongdari.

402 This humidification process below the UTCL should degrade the capacity of the UTCL
403 to sustain its low pressure and dry condition in the upper troposphere due to increases in
404 specific humidity at approximately 10 km altitude from 0.1 g kg^{-1} at the initial time to 0.6 g
405 kg^{-1} at 108 h at the center of the UTCL (Fig. 4a). This means that the low pressure of the
406 UTCL was hardly sustained due to the humidification process and thereby increases in
407 specific humidity in the UTCL. The increases in specific humidity (humidification) were
408 considered to be caused by cumulus convection over the warm ocean and its associated
409 diabatic heating since the interaction between the TC and the ocean plays a crucial role in
410 supplying heat and moisture from the ocean to the atmosphere and in transporting them
411 upward by cumulus convection around the TC and the edge of the UTCL. Given that the TC
412 intensity produced by the NHM was stronger than the best track TC intensity (Table 1), the
413 questions arise how ocean coupling processes affect the interaction between Jongdari and
414 the UTCL and how simulation results can better incorporate ocean coupling.

415 *3.4 Effect of ocean coupling on simulated Jongdari and UTCL*

416 Sea surface cooling such as that induced by Jongdari along its track, shown in Fig. 2,
417 is mainly caused by vertical turbulent mixing and upwelling in the upper ocean (Price 1981).
418 This fact suggests that the CPL or at least atmosphere-ocean coupled model is required to
419 reflect the dynamic and thermodynamic processes in simulations of Jongdari. An accurate

420 simulation of sea surface cooling requires an accurate atmospheric forcing to be applied to
421 the CPL as well as an accurate oceanic initial condition, particularly the stratification in the
422 upper ocean. In addition, the CPL needs to simulate surface wind speeds realistically. Here
423 we investigate the results simulated by the CPL in detail. The ocean waves simulated by the
424 CPL affect the roughness length over the ocean and thereby change the wind stress or
425 frictional velocity between the atmosphere and the ocean as well as the vertical turbulent
426 mixing caused by breaking waves (Wada et al. 2010).

427 Figure 10 maps the SST simulated by the CPL. The SST initial condition at 12 UTC
428 on 25 July successfully matches the observations shown in Fig. 2, an indication that the SST
429 initial condition was well created by interpolations in the simulations. However, the simulated
430 sea surface cooling induced by Jongdari was relatively weak because the simulated intensity
431 of Jongdari was weaker than the best track intensity even when the NHM was used (Table
432 1). The reason that the sea surface cooling was small as the TC moved rapidly westward is
433 that the vertical turbulent mixing beneath the TC had weakened owing to the weakening of
434 the atmospheric forcing.

435 Figure 11 maps hourly precipitation in simulations by the NHM and CPL at integration
436 times of 36, 72, and 108 h. The NHM simulated heavy rainfall around the TC center at 36 h
437 (Fig. 11a), and another area of precipitation was centered around 29°N, 145°E, where the
438 relative humidity on the 355 K isotherm was relatively high (see Fig. 9e). As Jongdari
439 approached land at 72 h, its center was an area of heavy rainfall, and narrow spiral

440 rainbands trailed it on its southeastern side (Fig. 11b). At 108 h, a concentric rainfall pattern
441 surrounded Jongdari as the TC redeveloped south of Kyushu (Fig. 11c). The simulation by
442 the CPL showed a small effect of ocean coupling on the distribution of hourly precipitation
443 at 36 h (Fig. 11d). At 72 and 108 h, however, the area of heavy precipitation became smaller
444 than in the noncoupled-model simulations (Figs. 11e, f). The presence of narrow spiral
445 rainbands below the UTCL during the integration reveals that local convection and
446 associated diabatic heating occurred below the UTCL.

447 Figure 12 maps latent heat fluxes from the ocean to the atmosphere simulated by
448 the NHM and CPL at integration times of 36, 72, and 108 h. The latent heat flux was relatively
449 high around the edge of cyclonic circulation and exceeded 400 W m^{-2} around the simulated
450 TC and along the south coast of Japan around 34.5°N, 139°E (Fig.12a). At 72 h, when the
451 simulated TC approached the Japanese archipelago, the latent heat flux exceeded 400 W
452 m^{-2} along the south coast of Japan around 34.5°N, 137°E, while the latent heat flux around
453 the edge of cyclonic circulation became smaller than before (Fig, 12b). At 108 h, the area of
454 latent heat flux exceeding 400 W m^{-2} was clearly found only within the inner core of simulated
455 TC (Fig. 12c). The difference in latent heat fluxes caused by ocean coupling was found
456 within the inner core of simulated TC at 36 h. The latent heat flux also decreased below the
457 UTCL around 32°N, 139°E although the amount of the decreases was relatively small. The
458 decrease in latent heat fluxes was found not only around the TC but also below the UTCL
459 around 30°N, 135°E (Figs. 12e, f). The area of the decreases in latent heat fluxes extended

460 from the limited TC area to the entire area below the UTCL as the integration time proceeded.
461 Hereinafter, it will be shown that the reduction in latent heat fluxes below the UTCL due to
462 ocean coupling helped suppress the convection and associated diabatic heating there.

463 Figure 13 corresponds to Fig. 7 except the results simulated by the CPL. At 36 h,
464 there was no significant difference between the noncoupled- and coupled-model simulations
465 of the distribution of pressure at approximately 10 km altitude or PV on the 355 K isotherm
466 (compare between Figs. 13a, b and Figs. 7d, e); however, the effect of ocean coupling
467 appeared in a decrease of the height of the PV tower of Jongdari and its magnitude
468 (compare Fig. 13c and Fig. 7f). In addition, ocean coupling decreased the upper-
469 tropospheric outflow by more than 10 m s^{-1} oriented from the top of the PV tower at 14-16
470 km and thus modified the locations of low-PV areas formed in the upper troposphere.

471 At 72 h, the pressure at 10 km altitude at the center of the UTCL was lower in the
472 coupled-model simulation (Fig. 13d) than in the noncoupled-model simulation (Fig. 7g). The
473 PV surrounding the UTCL was higher in the coupled-model simulation (Fig. 13e) than in the
474 noncoupled-model simulation (Fig. 7h). The height of PV tower was shorter in the coupled-
475 model simulation (Fig. 13f) than in the noncoupled-model simulation (Fig. 7i). These
476 differences due to ocean coupling were more apparent at 108 h (compare between Figs.
477 13g, h and Figs. 7j, k). They caused a delay in the coalescence of the UTCL and Jongdari:
478 In the noncoupled-model simulation, the PV tower extended from the surface to the
479 tropopause (‘V’ in Fig. 7l) and the tropopause folding tilted away from the PV tower (‘T’ in

480 Fig. 7l), whereas in the coupled-model simulation (Fig. 13i), the tropopause folding ('V' in
481 Fig. 13i) still tilted toward the PV tower ('T' in Fig. 13i).

482 Figure 14 shows the difference in geostrophic flows at approximately 10 km altitude
483 between the noncoupled- and coupled-model simulations with wind vectors indicating
484 geostrophic flows in the coupled-model simulation. The map of the difference in geostrophic
485 flows at 36 h (Fig. 14a) shows that the magnitude of geostrophic flows were almost the same
486 as those in the noncoupled-model simulation (Fig. 8b) although the magnitude around the
487 TC was ~25 m s^{-1} smaller in the coupled model simulation (Fig. 14a) than that in the
488 noncoupled-model simulation (Fig. 8b). The features were also found at 72 h (Fig. 14b).
489 However, the geostrophic-balanced cyclonic circulation was ~20 m s^{-1} stronger in the
490 coupled-simulations (Fig. 14b). At 108 h, the difference in geostrophic flows exceeded 20 m
491 s^{-1} only around the TC (Fig. 14c). Even though the locations of the TC and the UTCL
492 significantly differed between the noncoupled- and coupled-model simulations particularly at
493 the latter integration time (72 h and 108 h), the UTCL-induced geostrophic-balanced cyclonic
494 circulation was not clearly found east of simulated TC at 108 h so that it is hard to find the
495 direct impact of ocean coupling on the geostrophic-balanced cyclonic circulation.

496 Figure 15 corresponds to Fig. 9 except the results simulated by the CPL. At 36 h,
497 ocean coupling had produced no significant difference in the maps (compare Figs. 15a–c
498 and Figs. 9d–f) between the noncoupled- and coupled-model simulations except the area
499 around the PV tower where relative humidity was relatively high in the noncoupled-model

simulation.

At 72 h, the area where moisture flux exceeded 2 g m^{-2} s^{-1} at 10 km altitude around the circumference of the UTCL was larger (Fig. 15d). The area with less than 10% relative humidity on the 355 K isotherm around the UTCL was smaller (Fig. 15e) than in the noncoupled-model simulation (Figs. 9g, h), but the downward intrusion of dry air from the UTCL toward Jongdari was stronger above 12 km altitude in the coupled-model simulation ('X' in Fig. 15f) than that in the noncoupled-model simulation ('X' in Fig. 9i). At 108 h, the moisture flux at 10 km altitude near Jongdari was more widespread in the coupled-model simulation (compare Fig. 15g and Fig. 9j). Unlike the result at 72 h (Fig. 15e), an area with <10% relative humidity on the 355 K isotherm was apparent on the north side of Jongdari (Fig. 15h). In addition, the downward intrusion of dry air from the UTCL toward Jongdari was still apparent (Fig. 15i). Around the PV tower of Jongdari, the area with >70% relative humidity was higher than in the noncoupled-model simulation, exceeding 10 km altitude (compare Fig. 15i and Fig. 9l). This may partly result from the difference between the noncoupled- and coupled-model simulations in the structure of the PV tower and the nearby low-PV area in the area of upper-tropospheric outflow.

Our results demonstrate that adding ocean coupling to the atmosphere model helps reduce the PV around the PV tower of Jongdari. In addition, ocean coupling helps suppress warming of the air below the UTCL and thereby helps suppress the spread of decreased PV around the UTCL. The reduction due to ocean coupling in hourly precipitation below the

520 UTCL also reduces upper-tropospheric warming around the UTCL by the processes such
521 as reduction in latent heat fluxes from the ocean to the atmosphere, weakening convection
522 and associated diabatic heating particularly around the eyewall of the TC that moved along
523 the circumference of the UTCL, suppressing the production of areas of low PV in the upper
524 troposphere there and environmental effects that may help maintain high upper-level PV
525 around the UTCL. The reduction in PV around the outflow area of Jongdari, reduced upper-
526 troposphere warming around the UTCL, and the strengthened intrusion of dry air from the
527 UTCL to the vicinity of Jongdari due to relatively strong geostrophic-balanced cyclonic
528 circulation all were factors in delaying the coalescence of the UTCL and Jongdari. The delay
529 in the coalescence due to ocean coupling, interacting with the enlarged and strengthened
530 geostrophic-balanced cyclone circulation induced by the relatively strong UTCL, resulted in
531 a difference in the simulated track of Jongdari.

532 *3.5 Initial conditions and predictability*

533 The dry areas surrounding both the UTCL and Jongdari included the continental high,
534 the dry slot from the continental high, and another UTCL over the ocean east of Japan (Fig.
535 3) that appeared at 108 h integration time (Fig. 9k) when the initial time was 12 UTC on 25
536 July. The atmospheric environments at the initial time and those provided as lateral boundary
537 conditions differ depending on the initial time of integration, influencing the simulated track
538 and intensity of Jongdari. In fact, the simulated location (Fig. 4), intensity (Fig. 5a) and size
539 (Fig. 5b) of Jongdari differed greatly depending on the initial time of integration; the resulting

difference in track simulations was much greater than the difference caused by ocean coupling. In this section we compare the noncoupled-model and coupled-model simulations under initial conditions based on four different initial times.

Figure 16 shows the distribution of relative humidity and PV on the 355 K isotherm and the vertical cross section of PV on the line between the centers of Jongdari and the UTCL based on the JMA data at four times: 06 UTC, 12 UTC, and 18 UTC on 27 July and 00 UTC on 28 July. These were selected as initial times to provide an integration time of less than 72 h before 00 UTC on 30 July, the time at which Jongdari redeveloped south of Kyushu and coalesced with the UTCL (Fig. 7i). An integration time of less than 72 h was chosen to reduce the effect of ocean coupling on the simulations to some extent and to focus on the effect of the difference in atmospheric initial conditions.

At 06 UTC on 27 July, the UTCL with low relative humidity (Fig. 16a) and high PV (Fig. 16b) lay south of Japan. At that time, Jongdari was located southeast of the UTCL. The PV tower of Jongdari and the tropopause folding (>1 PV unit) from the UTCL lay along the vertical cross section, and they were approximately 500 km apart at 8 km altitude (Fig. 16c). At 12 UTC on 27 July, the UTCL had moved southward and Jongdari had moved cyclonically around the circumference of the UTCL compared to their positions 6 h earlier (Figs. 16d, e). The centers of Jongdari and UTCL were less than 500 km apart at 10 km altitude (Fig. 16f). At 18 UTC on 27 July, the dry area (Fig. 16g) with high PV was oriented northwest-southeast rather than north-south (Fig. 16h). Although the height of the PV tower was unchanged from

560 the simulation starting 6 h earlier (Fig. 16i), the area with high relative humidity on the 355
561 K isotherm had become concentrated near the center of Jongdari. At 00 UTC on 28 July,
562 Jongdari's motion had changed to west-northwestward while its maximum intensity matched
563 the best track central pressure (Fig. 5). The center of the UTCL coincided with the dry area
564 at the eastern edge of high PV area, and Jongdari had moved along the circumference of
565 the UTCL (Figs. 16j, k). The PV tower and the tropopause folding extending from the UTCL
566 were approximately 200 km apart at approximately 11 km altitude (Fig. 16l). The upward
567 motion was clear from the lower troposphere to the top of the PV tower, and the outflow from
568 the PV tower went to the southeast. In contrast, the winds from the tropospheric folding to
569 the PV tower were northwesterly. Overall, the behavior of the UTCL and Jongdari as
570 analyzed from different atmospheric initial conditions was continuous. It appears unfeasible
571 to detect a difference in the simulations that can be attributed to the atmospheric initial
572 conditions.

573 Figure 17 shows maps of relative humidity (Fig. 17a) and potential vorticity (Fig. 17b)
574 at the height of the 355 K isotherm and the vertical cross section of PV on the line AB shown
575 in Figs.17a, b (Fig. 17c) based on JMA 6-hourly global atmospheric analysis data at 00 UTC
576 on 30 July. Relative humidity was high west of TC within the inner core, whereas PV was
577 high east of TC. The height of the TC tower was approximately 8 km, and PV in the UTCL
578 was relatively high from 12 km to 14 km altitudes east of the TC.

579 Figure 18 corresponds to Fig. 16 except results of simulations by the NHM starting at

580 the four different initial times (i.e., at integration times of 48, 54, 60, and 66 h). All four
581 simulations featured a relatively dry area east-southeast of Jongdari (Fig. 18a) and high PV
582 on the 355 K isotherm (Fig. 18b) although the locations of high PV area relative to the TC
583 center were different from the global analysis particularly around the analyzed high PV area
584 at the height of the 355 K isotherm (Fig. 17b). The cross-section line in the noncoupled-
585 model simulation that started at 18 UTC on 27 July (Fig. 18g, h) differed from the others in
586 its orientation owing to the difference in the relative positions of Jongdari and the UTCL due
587 to the track error. In fact, the simulated track that started at 18 UTC on 27 July corresponds
588 to a track passing through Jeju Island in Fig. 4, which is approximately 227 km northwest of
589 the ensemble mean position. The relative positions of the tropopause folding and the PV
590 tower differed with the initial time of the integration (Figs. 18c, f, i, l). The shorter the
591 integration time, the closer the relative position to the analysis distribution. Note that the
592 heights of the PV tower in these four simulations were lower than the height in the
593 noncoupled-model simulation with the initial time of 12 UTC on 25 July (Fig. 7l), which
594 implies that the intensity of Jongdari was overestimated in the noncoupled-model simulation
595 with the earlier initial time. However, the heights of PV tower in all four simulations (Figs.
596 18c, f, i, l) were still higher (~10 km or higher) than the height of analyzed PV tower (~8 km)
597 (Fig. 17c). This suggests that the coalescence of Jongdari and the UTCL did not actually
598 occur and thus the coalescence in the noncoupled-model simulation starting at 12 UTC on
599 25 July was unrealistic.

600 The results of the coupled-model simulations at the four different initial times (Fig. 19)
601 differed somewhat from those of the noncoupled-model simulations (Fig. 16). The direction
602 of the cross-section line did not change due to ocean coupling, while the line clearly differs
603 among the four atmospheric initial conditions (compare Figs.18a, d, g, j and Figs. 19a, d, g,
604 j). This indicates that the atmospheric initial conditions determined the arrangement of
605 simulated Jongdari and UTCL and their evolutions. The high-PV area on the 355 K isotherm
606 southeast of Jongdari was slightly (from 10000 to 46000 km^2) larger due to ocean coupling
607 (Figs. 19b, e, h, k) except the simulated area that started at 18 UTC on 27 July (Fig. 19h).
608 The locations of high PV area relative to the TC center in the coupled-model simulations
609 (Figs. 19b, e, h, k) was closer to the location of analyzed high PV area (Fig. 17b) than those
610 in the noncoupled-model simulations (Figs.18b, e, h, k). The reduction in the amplitude of
611 positive PV in the PV tower was approximately 1.2 PVU (Fig. 19c), 0.2 PVU (Figs 19f, i) and
612 1.4 PVU (Fig. 19l) in the coupled-model simulations compared to that in the noncoupled-
613 model simulations. The height of simulated PV tower (Figs. 19c, f, I, l) became close to the
614 analyzed PV tower (Fig. 17c) due to the reduction caused by ocean coupling.
615 Although the geostrophic-balanced cyclonic circulation may dominate the TC
616 movement according to the analysis in Fig. 17, the simulated TC intensity was still
617 overdevelopment compared to the best track analysis even in the coupled-model
618 simulations. The excessively strong gradient winds of overdeveloped TC may be factors that
619 a large loop south of Kyusyu analyzed in the best track data shrank in the noncoupled- and

620 coupled-model simulations.

621 ## 4 Summary and discussion

622 We conducted numerical simulations of Typhoon Jongdari (2018) with the 3-km mesh
623 NHM and CPL, using different initial conditions from different initial times to investigate the
624 effects of the ocean and the atmospheric environment on the storm's irregular and unusual
625 track. We also investigated the interactions between Jongdari and the UTCL in detail to
626 understand the relation of their intensities to their respective tracks.

627 In the early intensification phase, Jongdari lay on the south-southeastern edge of the
628 UTCL, represented by high PV on the 355 K isotherm. While the UTCL moved
629 southwestward, Jongdari moved north-northeastward and then moved cyclonically along the
630 western edge of the UTCL. When the UTCL slowed as it stayed south of Japan, Jongdari
631 moved across the northern edge of the geostrophic-balanced cyclonic circulation induced
632 below the UTCL, where mid-tropospheric relative humidity was high. In Jongdari's mature
633 phase, the storm induced sea surface cooling along its track. Jongdari weakened after
634 landfall in Japan as the UTCL also weakened, staying south of Japan. After Jongdari moved
635 west over the Japanese archipelago, it redeveloped over the ocean south of Kyushu.

636 The NHM simulation with the earliest initial time (12 UTC on 25 July) showed that the
637 simulated intensity of TC tended to be overdevelopment compared to the best track analysis.
638 During the southwestward movement of UTCL, the cyclonic loop of TC track was controlled
639 by the UTCL-induced geostrophic-balanced cyclonic circulation, while the UTCL was

640 weakening by humidification caused by cumulus convection over the warm ocean and
641 associated diabatic heating. The PV tower of simulated Jongdari appeared to merge with
642 the UTCL south of Kyushu and thus TC motion simulated by the NHM may be controlled by
643 excessively strong gradient winds of overdeveloped TC rather than the UTCL-induced
644 geostrophic-balanced cyclonic circulation.

645 The corresponding simulation by the CPL showed an increased PV in the tropopause
646 around the UTCL and a decreased PV at the PV tower. The increased PV in the upper
647 troposphere represented by PV on the 355 K isotherm could be accounted for by reduced
648 hourly precipitation below the UTCL due to ocean coupling, which resulted in less warming
649 in the upper troposphere around the UTCL, because of (1) reduced latent heat flux, (2)
650 weakened cumulus convection over the cooled ocean and reduced diabatic heating
651 particularly around the eyewall of TC and partly below the UTCL, (3) suppressed production
652 of the low-PV area in the upper troposphere around the UTCL and (4) environmental effects
653 that may help maintain high upper-level PV around the UTCL. Ocean coupling suppressed
654 the upper-tropospheric outflow at the top of the PV tower, which affected the location of low
655 upper-tropospheric PV and thus helped sustain the amplitude of the PV in the tropopause
656 around the UTCL. Finally, ocean coupling led to reduction in PV within the PV tower, which
657 helped avoid the coalescence of Jongdari and the UTCL. Thus, ocean coupling affected the
658 simulation of Jongdari's track through modifications of the intensities of both Jongdari and
659 UTCL although the TC intensity simulated by the CPL was still overdevelopment compared

660 to the best track analysis so that a large loop south of Kyusyu analyzed in the best track
661 data shrank in the coupled-model simulations due to relatively strong gradient winds. A new
662 finding of this study is that the intensity of not only the TC but also the UTCL is affected by
663 ocean coupling. This study also showed that this modification of intensities modified the
664 interactions between the TC and the UTCL to affect the simulated TC track.

665 Our simulations show that differences in the initial conditions lead to errors in the
666 simulated Jongdari track that originate in differences in the synoptic environments such as
667 the UTCL, the continental high, the dry slot from the continental high, and another UTCL
668 over the ocean east of Japan. When the effects of ocean coupling are added to these, the
669 track simulation of Jongdari is further perturbed by affecting the interactions between
670 Jongdari and the UTCL through the change in their respective intensities. Figure 20
671 summarizes characteristics of atmospheric and oceanic environments, the interactions
672 between the TC and UTCL, and the effect of ocean coupling as a schematic diagram. The
673 addition of ocean coupling improves Jongdari simulations by weakening the PV tower and
674 increasing the PV in the UTCL. On the other hand, our results suggest that the error in
675 simulating the intensity of Jongdari, attributed to the error of the synoptic environment at the
676 initial integration time, may in turn affect the simulation of the atmospheric environment itself
677 and lead to increased errors in TC simulations. Our results suggest that the TC simulations
678 are much more sensitive to atmospheric initial environments than to ocean coupling.
679 Although the effect of ocean coupling on the behavior of the UTCL may be important for

680 improving the accuracy of TC simulations, further systematic research is needed on the
681 effects of atmospheric initial conditions on TC simulations while at the same time making
682 improvements in atmospheric analysis.
683
684 **Acknowledgments**
685 The author appreciates Prof. T. Sato and two anonymous reviewers for comments that help
686 improve the first manuscript. Generic Mapping Tools software (http://gmt.soest.hawai.edu/)
687 was used to draw the figures. This study was supported by Grants-in-Aid for Scientific
688 Research (KAKENHI) Numbers JP19H01973 and JP19H05696 from the Japan Society for
689 the Promotion of Science.
690
691 **References**
692 Agusti‐Panareda, A., C. D. Thorncroft, G. C. Craig, and S. L. Gray, (2004) The
693 extratropical transition of hurricane Irene (1999): A potential‐vorticity perspective.
694 *Q.J.R. Meteorol. Soc.*, **130**, 1047-1074.
695 Bender, M. A., I. Ginis, and Y. Kurihara, (1993). Numerical simulations of tropical cyclone–
696 ocean interaction with a high–resolution coupled model. *J. Geophys. Res.*, **98**, 23245–
697 23263.
698 Bosart, L. F. (2003) Tropopause folding, upper-level frontogenesis, and beyond. A Half
699 Century of Progress in Meteorology: A Tribute to Richard J. Reed. *Meteor. Monogr.*, **53**,

13–47.

Davis, C. A., and K. A. Emanuel, (1991). Potential vorticity diagnostics of cyclogenesis, *Mon. Weather Rev.*, **119**, 1929-1953.

Deardorff, J. W., 1980: Stratocumulus-capped mixed layers derived from a three-dimensional model. *Bound.-Layer Meteor.*, **18**, 495-527.

Fierro, A. O., R. F. Rogers, F. D. Marks, and D. S. Nolan, (2009). The impact of horizontal grid spacing on the microphysical and kinematic structures of strong tropical cyclones simulated with the WRF–ARW model. *Mon. Weather Rev.*, **137**, 3717– 3743.

Gaiser, P. W., Germain, K. M. S., Twarog, E. M., Poe, G. A., Purdy, W., Richardson, D., Grossman, W., Jones, W. L., Spencer, D., Golba, G., Cleveland, J., Choy, L., Bevilacqua, R. M., and Chang, P. S., 2004: The WindSat spaceborne polarimetric microwave radiometer: Sensor description and early orbit performance. *IEEE Trans. Geosci. Remote Sens.*, **42**, 2347–2361.

Gimeno, L., R. M. Trigo, R. Ribera, and J. A. Garcia, (2007) Editorial: special issue on cut-off low systems (COL), *Meteorol. Atmos. Phys.*, **96**, 1-2.

Ikawa, M., and K. Saito, (1991) Description of a nonhydrostatic model developed at the forecast research department of the MRI. Tech. Rep. of the MRI, 28, 238 pp.

Ito, K., T. Kuroda, K. Saito, and A. Wada, (2015) Forecasting a large number of tropical cyclone intensities around Japan using a high-resolution atmosphere-ocean coupled model, *Wea. Forecasting*, **30**, 793-808.

720 Jones, S. C. (1995) The evolution of vortices in vertical shear. Part I: Initially barotropic
721 vortices. *Quart. J. Roy. Meteor. Soc.*, **121**, 821–852.
722 Kanada, S., and A. Wada, (2016). Sensitivity to horizontal resolution of the simulated
723 intensifying rate and inner–core structure of typhoon Ida: An extremely intense typhoon.
724 *J. Meteor. Soc. Japan*, **94A**, 181– 190.
725 Klemp, J. B., and R. Wilhelmson, (1978) The simulation of three-dimensional convective
726 storm dynamics. *J. Atmos. Sci.*, **35**, 1070-1096.
727 Kondo, J., (1975) Air-sea bulk transfer coefficients in diabatic conditions. *Bound.-Layer*
728 *Meteor.*, **9**, 91-112.
729 Kuo, Y.-C., Z.-W. Zheng, Q. Zheng, G. Gopalakrishnan, H.-Y., Lee, (2018) Typhoon–
730 Kuroshio interaction in an air–sea coupled system: Case study of typhoon nanmadol
731 (2011), *Ocean Modelling*, **132**, 130-138.
732 Lander, M. A. (1994) Description of a Monsoon Gyre and Its Effects on the Tropical
733 Cyclones in the Western North Pacific during August 1991, *Wea. Forecasting*, **9**, 640-
734 654.
735 Lei, L., Y. Ge, Z. Tan, and X. Bao, (2020) An evaluation and improvement of tropical
736 cyclone prediction in the western North Pacific basin from global ensemble forecasts.
737 *Sci. China Earth Sci.* **63**, 12–26.
738 Lin, Y.-L., R. D. Farley, and H. D. Orville, (1983) Bulk parameterization of the snow field in
739 a cloud model. *J. Appl. Meteor. Climatol.*, **22**, 1065-1092.

740 Miyamoto, Y., M. Satoh, H. Tomita, K. Oouchi, Y. Yamada, C. Kodama, and J., III., Kinter,
741 (2014) Gradient wind balance in tropical cyclones in high-resolution global experiments,
742 *Mon. Weather Rev.*, **142**, 1908-1926.
743 Mogensen, K. S., L. Magnusson, and J.-R. Bidlot, (2017) Tropical cyclone sensitivity to
744 ocean coupling in the ECMWF coupled model. *J. Geophys. Res. Oceans*, **122**, 4392–
745 4412.
746 Molinari, J, S. Skubis, D. Vollaro, F. Alsheimer, and H. E. Willoughby, (1998) Potential
747 vorticity analysis of tropical cyclone intensification. *J. Atmos. Sci.*, **55**, 2632-2644.
748 Nieto, R., L. Gimeno, L. de la Torre, P. Ribera, D. Gallego, R. G.-Herrera, J. A. García, M.
749 Nuňez, A. Redaňo, and J. Lorente, (2005) Climatological feature of cutoff low systems in
750 the northern hemisphere, *J. Climate*, **18**, 3085–3103.
751 Nieto, R., M. Sprenger, H. Wernli, R. M. Trigo, and L. Gimeno, (2008) Identification and
752 Climatology of cut-off lows near the tropopause, *Ann. N. Y. Scad. Sci.*, **1146**, 256-290.
753 Ohlmann, J. C., and D. A. Siegel, (2000) Ocean radiant heating. Part II: Parameterizing
754 solar radiation transmission through the upper ocean, *J. Phys. Oceanogr.*, **30**, 1849-
755 1865.
756 Oyama, R. and A. Wada, (2019) The relationship between convective bursts and warm-
757 core intensification in a nonhydrostatic simulation of Typhoon Lionrock (2016). *Mon.*
758 *Weather Rev.*, **147**, 1557–1579.
759 Patla, J. E., D. Stevens, and G. M. Barnes, (2009) A conceptual model for the influence of

760 TUTT cells on tropical cyclone motion in the Northwest Pacific Ocean. *Wea.*
761 *Forecasting*, **24**, 1215-1235.
762 Price, J. F., (1981) Upper ocean response to a hurricane. *J. Phys. Oceanogr.*, **11**, 153-175.
763 Price, J. D., and G. Vaughan, (1993) The potential for stratosphere-troposphere exchange
764 in cut-off-low systems. *Q.J.R. Meteorol. Soc.*, **119**, 343-365.
765 Sadler, J. C. (1976) A role of the tropical upper tropospheric trough in early season
766 typhoon development. *Mon. Weather Rev.*, **104**, 1266-1278.
767 Sadler, J. C. (1978) Mid-season typhoon development and intensity changes and the
768 tropical upper tropospheric trough. *Mon. Weather Rev*., **106**, 1137-1152.
769 Saito, K. (2012). The JMA nonhydrostatic model and its applications to operation and
770 research. In I. Yucel (Ed.), Atmospheric model applications (pp. 85– 110). Croatia:
771 InTech.
772 Schiller, A., and J. S. Godfrey, (2005) A diagnostic model of the diurnal cycle of sea
773 surface temperature for use in coupled ocean-atmosphere models, *J. Geophys. Res.*,
774 **110**, C11014.
775 Shapiro, L. J. (1992) Hurricane vortex motion and evolution in a three-layer model. *J.*
776 *Atmos. Sci.*, **49**, 140–153.
777 Sugi, M., K. Kuma, K. Tada, K. Tamiya, N. Hasegawa, T. Iwasaki, S. Yamada, and T.
778 Kitade, (1990) Description and performance of the JMA operational global spectral
779 model (JMA-GSM88). *Geophys. Mag.*, **43**, 105-130.

780 Taylor, P. K., and M. J. Yelland, (2001) The dependence of sea surface roughness on the
781 height and steepness of the waves. *J. Phys. Oceanogr.*, **31**, 572-590.
782 Wada, A., (2021) Roles of oceanic mesoscale eddy in rapid weakening of Typhoons Trami
783 and Kong-Rey in 2018 simulated with a 2-km-mesh atmosphere-wave-ocean coupled
784 model. *J. Meteor. Soc. Japan,* **99**, in press.
785 Wada, A., (2017) Sensitivity numerical simulations of Hurricane Patricia (2015) on lateral
786 boundary conditions and inhibition rate of evaporation. *CAS/JSC WGNE Res. Activ.*
787 *Atmos. Oceanic Modell.*, **47**, 0522-0523.
788 Wada, A., and M. Kunii, (2017) The role of ocean–atmosphere interaction in Typhoon
789 Sinlaku (2008) using a regional coupled data assimilation system. *J. Geophys. Res.*
790 *Oceans,* **122**, 3675– 3695.
791 Wada, A., and R. Oyama, (2018) Relation of convective bursts to changes in the intensity
792 of Typhoon Lionrock (2016) during the decay phase simulated by an atmosphere-wave-
793 ocean coupled model. *J. Meteor. Soc. Japan,* **96**, 489-509.
794 Wada, A., S. Kanada, and H. Yamada, (2018) Effect of air-sea environmental conditions
795 and interfacial processes on extremely intense typhoon Haiyan (2013). *J. Geophys.*
796 *Res.*, **123**, 10379-10405.
797 Wada, A, N. Kohno, and Y. Kawai, (2010) Impact of wave-ocean interaction on Typhoon
798 Hai-Tang in 2005. *SOLA*, **6A**, 13–16.
799 Wang, Y., and C.–C. Wu, (2004) Current understanding of tropical cyclone structure and

intensity change—A review. *Meteorol. Atmos. Phys*., **87**, 257– 278.

Wei, N., Y. Li, D. Zhang, Z. Mai, and S. Yang, (2016) A statistical analysis of the relationship between upper-tropospheric cold low and tropical cyclone track and intensity change over the western North Pacific, *Mon. Weather Rev.*, 144, 1805-1822.

Welander, P. (1955) Studies on the general development of motion in a two-dimensional ideal fluid. *Tellus*, **7**, 141-156.

Wu, C.-C., and K. A. Emanuel, (1993) Interaction of a baroclinic vortex with background shear: Application to hurricane movement. *J. Atmos. Sci.*, **50**, 62–76.

Wu, C.−R., Y.-L. Chang, L.-Y. Oey, C.-W. J. Chang, and Y.-C. Hsin, (2008) Air−sea interaction between tropical cyclone Nari and Kuroshio, *Geophys. Res. Lett.*, **35**, L12605.

Yan, Z., X. Ge, Z. Wang, C.-C.Wu, and M. Peng (2021) Understanding the impacts of upper-tropospheric cold low on Typhoon Jongdari (2018) using piecewise potential vorticity inversion, *Mon. Weather Rev.*, doi:10.1175/MWR-D-20-0271.1.

List of Figures

Fig.1 JMA weather maps at 00 UTC on (a) 26 July, (b) 27 July, (c) 28 July, (d) 29 July, (e) 30 July, and (f) 31 July 2018. Contour intervals are 4 hPa for solid isobars and 2 hPa for dashed isobars. TD, tropical depression; TS, tropical storm; L (H), area where sea-level pressure is lower (higher) than the surroundings.

Fig.2 Daily SST (colors in the right-hand color bar) from 25 July to 1 August 2018 with best

820 track positions of Jongdari every 6 h (circles). Colors of the circles (left-hand color bar)
821 indicate the best track central pressure. The large circle indicates the position of Jongdari
822 at the time of the plot.
823 Fig.3 Brightness temperatures (Band 13, gray scale) and atmospheric motion vectors
824 (arrows; red arrow represents 30 m s^{-1}) between 250 and 350 hPa heights at 12 UTC
825 from 25 July to 1 August. Red circles indicate the position of Jongdari, and the color
826 indicates the minimum central pressure. The letter C from 12 UTC on 25 July to 12 UTC
827 on 27 July indicates the location of the UTCL.
828 Fig.4 Simulations by the NHM (a, c) and CPL (b, d). (a, b) Blue thick line with circles (colors
829 indicate the central pressure) and error bars (one standard deviation) show the ensemble
830 mean TC tracks at 12 h intervals. Black thick line with diamonds shows best track TC
831 positions at 12 h intervals. Red thick line with stars (colors indicate the temperature) and
832 error bars (one standard deviation) shows locations of the UTCL at 12 h intervals. ‘A’ (12
833 UTC on 25 July), ‘B’ (06 UTC on 27 July), ‘C’ (12 UTC on 27 July), ‘D’, (18 UTC on 27
834 July), ‘E’ (00 UTC on 28 July) with thin lines indicate the simulated TC track, whereas ‘a’
835 (12 UTC on 25 July), ‘b’ (06 UTC on 27 July), ‘c’ (12 UTC on 27 July), ‘d’, (18 UTC on 27
836 July), ‘e’ (00 UTC on 28 July) with thin lines indicate the simulated locations of UTCL in at
837 each initial time. (c, d) The relative position evolutions between TC (origin, red mark) and
838 UTCL (the end of the arrow) from 12 UTC on 25 July to 12 UTC on 31 July. Each two digit
839 depicted in each panel as four digits mean day and time (UTC).

840 Fig.5 (a) Time series showing the best track central pressure (gray circles), ensemble
841 mean central pressures with the error bar (one standard deviation) simulated by the
842 NHM (red circles with the vertical line) and the atmosphere-wave-ocean coupled model
843 (light blue circles with the vertical line) and simulated central pressures with atmospheric
844 initial conditions at 12 UTC on 25 July, 06, 12, 18 UTC on 27 July and 00 UTC on 28
845 July. See Table 1 for the identity of the different simulations. (b) Time series showing
846 ensemble mean radius of the maximum winds at 20-m height with the error bar (one
847 standard deviation) simulated by the NHM (red circles with the vertical line) and CPL
848 (light blue circles with the vertical line).
849 Fig.6 (Left) Mean track errors with respect to the best track position and (right) central
850 pressure errors with respect to the mean best track central pressure in the noncoupled-
851 model simulations (red circles and lines), and coupled-model simulations (blue circles and
852 lines). The error bars indicate one standard deviation.
853 Fig.7 Simulations by the NHM with initial conditions at 12 UTC on 25 July at integration times
854 of (a–c) 0 h, (d–f) 36 h, (g–i) 72 h, and (j–l) 108 h. Left panels show the distribution of
855 pressure at approximately 10 km altitude (colors), sea-level pressure (black lines, contour
856 interval 8 hPa), and wind vectors at approximately 10 km altitude. Center panels show the
857 distribution of PV (colors) and wind vectors on the 355 K isotherm. Right panels show a
858 vertical profile of PV (colors), potential temperature (black lines, interval 10 K), and
859 horizontal-vertical wind vectors parallel to the cross section along the line between the

centers of Jongdari and the UTCL (see section 3.2), shown as dashed lines in the left and center panels. "A-H" indicate the location of the start and end points of the cross section. ‘T’ and ‘V’ in Fig. 7l are explained in the text.

Fig. 8 Horizontal distribution of the magnitude of geostrophic flow on the 355 K isotherm (colors), sea-level pressure (purple lines, contour interval 8 hPa), and geostrophic flow vectors on the 355 K isotherm simulated by the NHM with initial conditions at 12 UTC on 25 July at integration times of (a) 0 h, (b) 36 h, (c) 72 h, and (d) 108 h.

Fig.9 Simulations by the NHM with initial conditions at 12 UTC on 25 July at integration times of (a–c) 0 h, (d–f) 36 h, (g–i) 72 h, and (j–l) 108 h. Left panels show the distributions of horizontal moisture flux (colors) at approximately 10 km altitude. Center panels show relative humidity on the 355 K isotherm (colors). Right panels show a vertical profile of relative humidity (colors), potential temperature (black lines, interval 10 K), and horizontal-vertical wind vectors parallel to the cross section along the line between the centers of Jongdari and the UTCL shown as white lines in the left and center panels. "A-H" indicate the location of the start and end points of the cross section. ’X’ in Fig. 9i is explained in the text.

Fig.10 Horizontal distribution of SST simulated by the CPL from 25 July to 1 August with initial conditions at 12 UTC on 25 July and simulated positions of Jongdari every 6 h (circles). The large circle indicates the simulated position of Jongdari at the time of the plot. Colors of the circles indicate the simulated central pressure.

880 Fig.11 Distributions of hourly precipitation (colors) and sea-level pressure (contours, interval
881 8 hPa) in the noncoupled-model simulation at integration times of (a) 36 h, (b) 72 h, and
882 (c) 108 h and in the coupled-model simulation at integration times of (d) 36 h, (e) 72 h,
883 and (f) 108 h.
884 Fig.12 Distributions of latent heat flux (colors) and sea-level pressure (contours, interval 8
885 hPa) in the noncoupled-model simulation at integration times of (a) 36 h, (b) 72 h, and (c)
886 108 h and in the coupled-model simulation at integration times of (d) 36 h, (e) 72 h, and
887 (f) 108 h.
888 Fig.13 Simulations by the CPL with initial conditions at 12 UTC on 25 July at integration
889 times of (a–c) 36 h, (d–f) 72 h, and (g–i) 108 h, corresponding to the noncoupled-model
890 simulation in Fig. 7. Symbols and colors are the same as Fig. 7. ‘T’ and ‘V’ in Fig. 13i are
891 explained in the text.
892 Fig.14 Horizontal distributions in the difference in magnitude (colors) and vector (arrows) of
893 geostrophic flows between the noncoupled-model simulations and the coupled-model
894 simulations (CPL minus NHM) with initial conditions at 12 UTC on 25 July at integration
895 times of (a) 36 h, (b) 72 h, and (c) 108 h. The contours indicate sea-level pressure
896 simulated by the CPL. The interval is 8 hPa.
897 Fig.15 Simulations by the CPL with initial conditions at 12 UTC on 25 July at integration
898 times of (a–c) 36 h, (d–f) 72 h, and (g–i) 108 h, corresponding to the noncoupled-model
899 simulation in Fig. 9. Symbols and colors are the same as Fig. 9. ’X’ in Fig. 15f is explained

900 in the text.

901 Fig.16 Atmospheric conditions based on JMA data at four different times: (a–c) 06 UTC on
902 27 July, (d–f) 12 UTC on 27 July, (g–i) 18 UTC on 27 July, and (j–l) 00 UTC on 28 July.
903 These were used as initial conditions for simulations ending at 00 UTC on 30 July (see
904 text). Left panels show the distribution of relative humidity on the 355 K isotherm (colors),
905 wind vectors at that altitude, and sea-level pressure (black lines, contour interval 8 hPa).
906 Center panels show the distribution of PV (colors) and sea-level pressure (black lines,
907 contour interval 8 hPa). Right panels show a vertical profile of PV (colors), potential
908 temperature (black lines, interval 10 K), and horizontal-vertical wind vectors parallel to the
909 cross section along the line between the centers of Jongdari and the UTCL (see section
910 3.2), shown as dashed lines in the left and center panels. "A-H" indicate the location of
911 the start and end points of the cross section.

912 Fig.17 Atmospheric conditions based on JMA 6-hourly global atmospheric analysis data at
913 00 UTC on 30 July. (a) The distribution of relative humidity on the 355 K isotherm (colors),
914 wind vectors at that altitude, and sea-level pressure (purple lines, contour interval 8 hPa).
915 (b) The distribution of PV (colors) and sea-level pressure (black lines, contour interval 8
916 hPa). (c) A vertical profile of PV (colors), potential temperature (black lines, interval 10 K),
917 and horizontal-vertical wind vectors parallel to the cross section along the line between
918 the centers of Jongdari and the UTCL (see section 3.2), shown as dashed lines in the left
919 and center panels.

Fig.18 Results of simulations by the NHM at 00 UTC on 30 July from the initial conditions in Fig. 16.

Fig.19 Results of simulations by the CPL at 00 UTC on 30 July from the initial conditions in Fig. 16.

Fig.20 Schematic diagrams depicting the interactions between Jongdari and the UTCL (hatched solid boxes) addressed in this study. Factors associated with uncertainty of atmospheric environments and ocean coupling are shown. Solid boxes shows factors addressed in this study. SST and difference in atmospheric initial conditions are shaded. Solid ellipses indicate the comparison of geostrophic and gradient winds that affect simulated TC tracks between the noncoupled- and coupled-model simulations. Dashed boxes show the comparison regarding the factor in each solid box. Humidification indicated in large arrows is directly affected by diabatic heating and the effect is accumulated in the atmospheric environments, resulting in the impact on UTCL. Difference in atmospheric environments at the initial time indicated in another large arrow is also one of the atmospheric environment factors that affects the simulations of TC and UTCL.

Table 1 Locations, central pressures (hPa), and maximum wind speeds (m s^{-1}) of Jongdari averaged for 144-h integration times calculated from simulation results starting from each initial time. In the left column, B represents best track data (BEST); A, simulation results from the NHM; and AWO, simulation results from the CPL. The numerals *mmddhh* represent the initial time as follows: *mm*, month in 2018; *dd*, day; and *hh*, hour (UTC).

	Longitude(average)	Latitude(average)	Central pressure (average)	maximum wind speed (average)
BEST				
B072512	138.91	28.35	974.76	31.62
B072518	138.47	28.95	975.00	31.17
B072600	137.98	29.49	975.53	30.56
B072606	137.47	29.97	976.06	29.96
B072612	136.91	30.36	976.59	28.29
B072618	136.37	30.70	977.41	26.48
B072700	135.82	31.05	979.00	25.42
B072706	135.19	31.38	980.76	24.21
B072712	134.39	31.64	982.24	23.15
B072718	133.46	31.79	983.71	22.09
B072800	132.50	31.78	985.47	20.88
B072806	131.56	31.62	987.24	19.67
B072812	130.74	31.34	988.71	18.61
mean	**135.37**	**30.65**	**980.19**	**25.54**
NHM				
A072512	135.81	28.82	976.18	34.49
A072518	135.62	28.76	962.57	41.13
A072600	135.21	29.24	965.71	40.43
A072606	134.80	29.40	965.96	39.33
A072612	134.31	30.10	967.06	38.88
A072618	133.37	30.60	970.71	35.32
A072700	133.07	30.36	964.30	38.54
A072706	132.19	30.86	975.90	31.67
A072712	131.48	31.19	981.12	29.12
A072718	130.74	31.62	987.12	24.86
A072800	130.11	31.29	984.00	26.90
A072806	131.58	30.08	978.39	29.53
A072812	130.31	30.78	981.73	28.37
mean	**132.97**	**30.24**	**973.90**	**33.74**
CPL				
AWO072512	135.76	28.93	980.61	29.39
AWO072518	135.81	28.62	971.01	33.07
AWO072600	135.11	29.31	974.69	32.17
AWO072606	135.01	29.26	973.39	31.15
AWO072612	134.36	30.11	973.75	32.59
AWO072618	133.51	30.56	972.87	31.11
AWO072700	132.96	30.61	972.60	31.11
AWO072706	132.36	30.77	977.16	28.10
AWO072712	131.58	31.24	984.12	25.40
AWO072718	131.68	31.69	989.14	22.12
AWO072800	131.16	30.80	985.93	23.82
AWO072806	131.68	30.13	984.05	24.37
AWO072812	131.92	29.60	981.48	25.69
mean	**133.30**	**30.13**	**978.52**	**28.47**

944

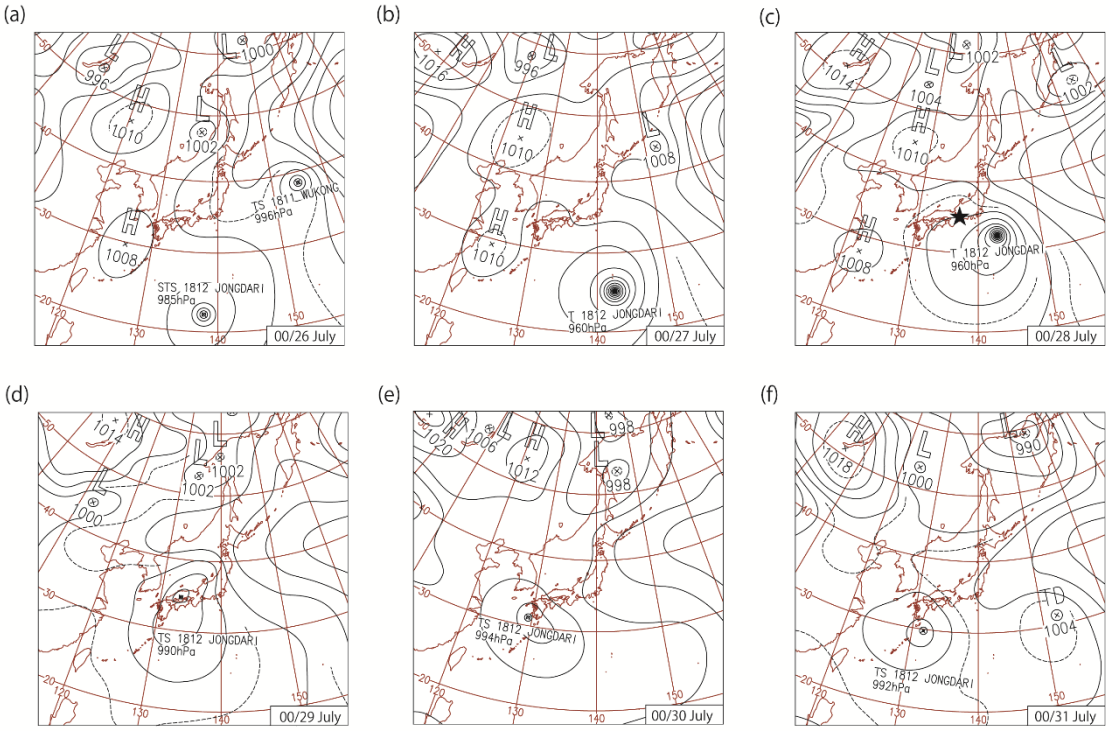

Fig.1 JMA weather maps at 00 UTC on (a) 26 July, (b) 27 July, (c) 28 July, (d) 29 July, (e) 30 July, and (f) 31 July 2018. Contour intervals are 4 hPa for solid isobars and 2 hPa for dashed isobars. TD, tropical depression; TS, tropical storm; L (H), area where sea-level pressure is lower (higher) than the surroundings.

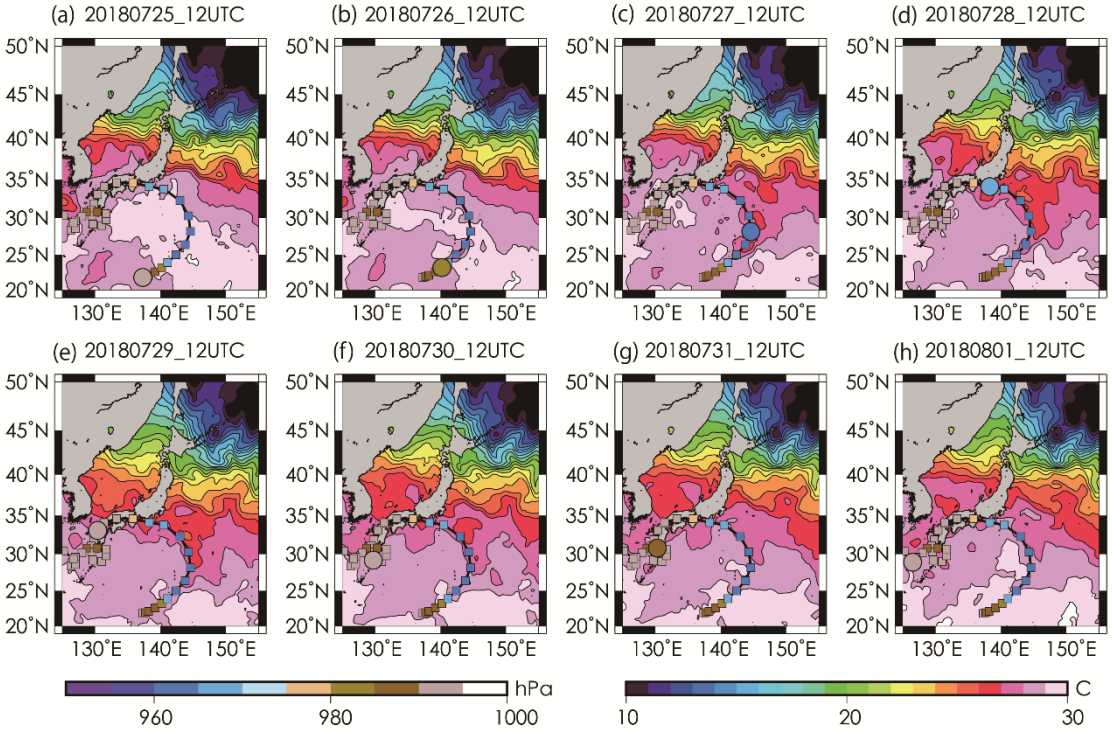

Fig.2 Daily SST (colors in the right-hand color bar) from 25 July to 1 August 2018 with best track positions of Jongdari every 6 h (circles). Colors of the circles (left-hand color bar) indicate the best track central pressure. The large circle indicates the position of Jongdari at the time of the plot.

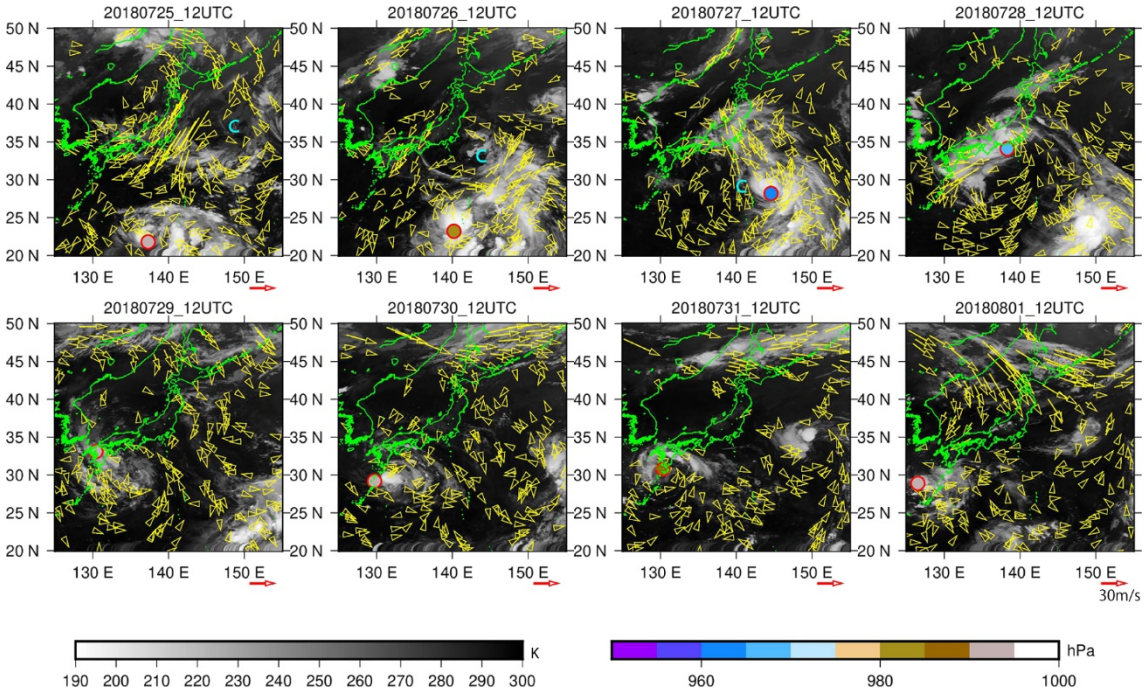

Fig.3 Brightness temperatures (Band 13, gray scale) and atmospheric motion vectors (arrows; red arrow represents 30 m s^{-1}) between 250 and 350 hPa heights at 12 UTC from 25 July to 1 August. Red circles indicate the position of Jongdari, and the color indicates the minimum central pressure. The letter C from 12 UTC on 25 July to 12 UTC on 27 July indicates the location of the UTCL.

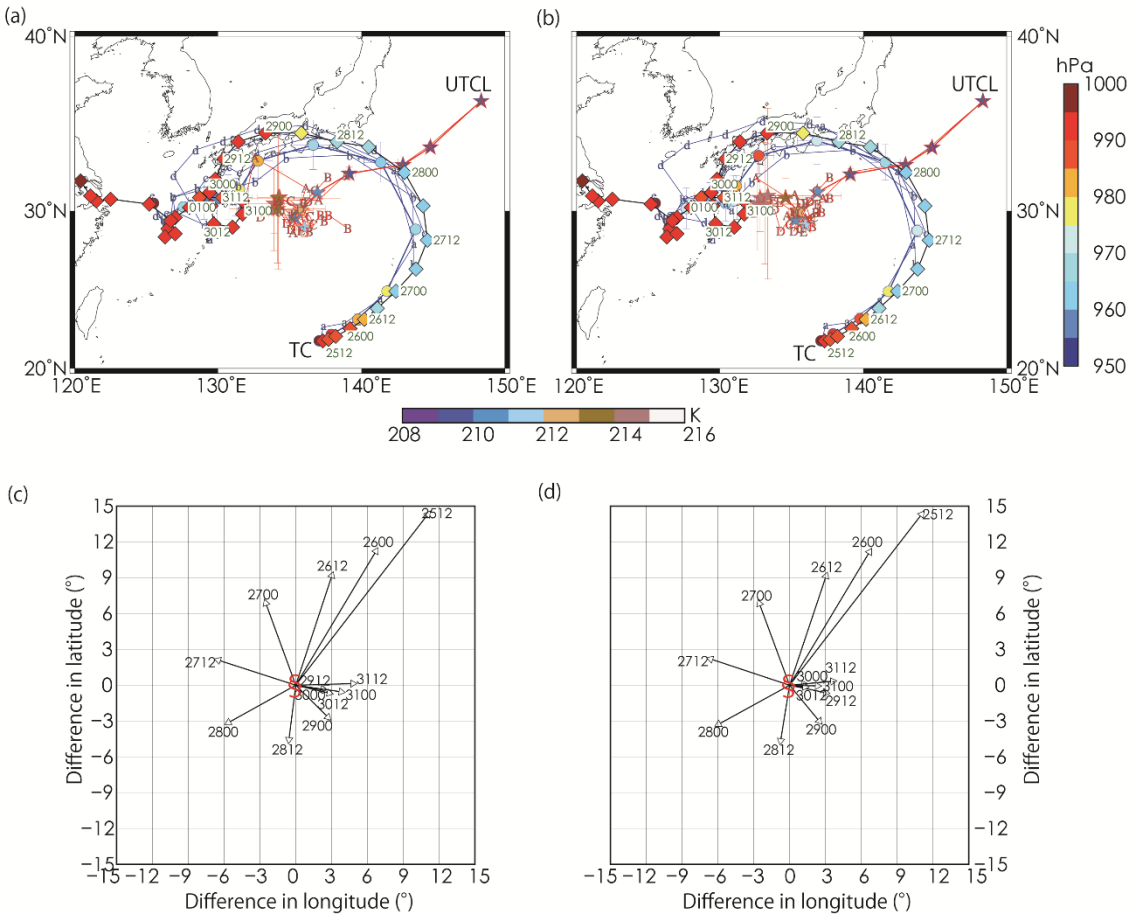

Fig.4 Simulations by the NHM (a, c) and CPL (b, d). (a, b) Blue thick line with circles (colors indicate the central pressure) and error bars (one standard deviation) show the ensemble mean TC tracks at 12 h intervals. Black thick line with diamonds shows best track TC positions at 12 h intervals. Red thick line with stars (colors indicate the temperature) and error bars (one standard deviation) shows locations of the UTCL at 12 h intervals. 'A' (12 UTC on 25 July), 'B' (06 UTC on 27 July), 'C' (12 UTC on 27 July), 'D', (18 UTC on 27 July), 'E' (00 UTC on 28 July) with thin lines indicate the simulated TC track, whereas 'a' (12 UTC on 25 July), 'b' (06 UTC on 27 July), 'c' (12 UTC on 27 July), 'd', (18 UTC on 27 July), 'e' (00 UTC on 28 July) with thin lines indicate the simulated locations of UTCL in at each initial time. (c, d) The relative position evolutions between TC (origin, red mark) and UTCL (the end of the arrow) from 12 UTC on 25 July to 12 UTC on 31 July. Each two digit depicted in each panel as four digits mean day and time (UTC).

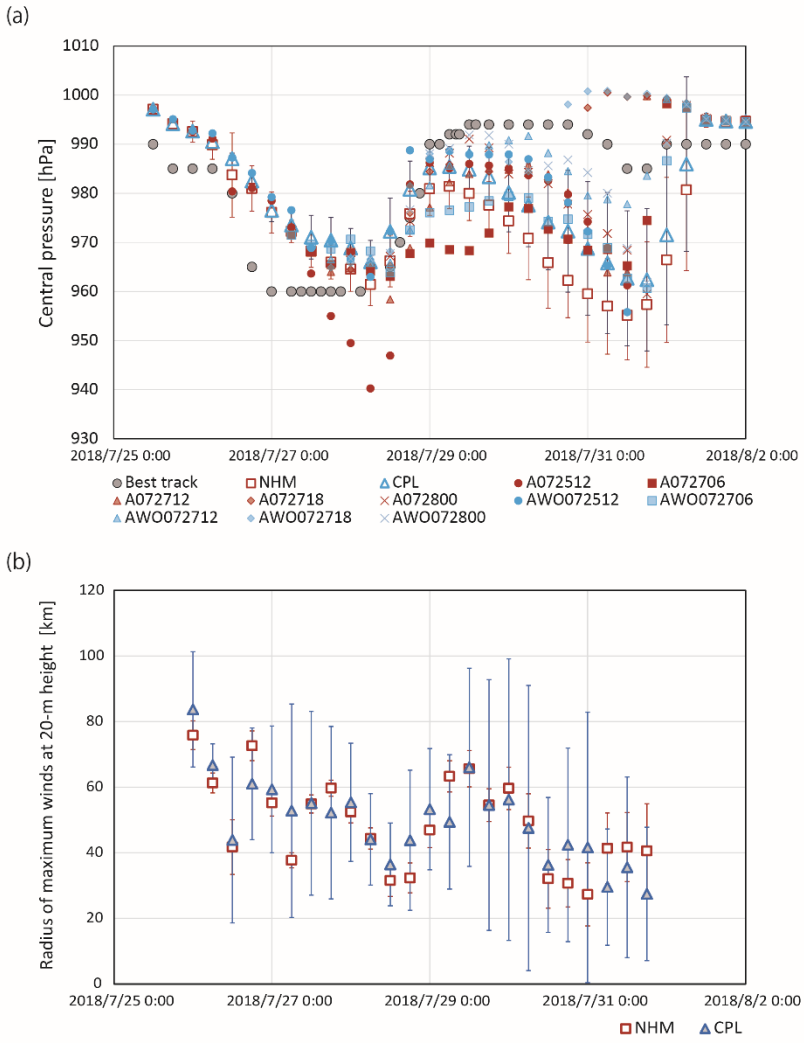

Fig.5 (a) Time series showing the best track central pressure (gray circles), ensemble mean central pressures with the error bar (one standard deviation) simulated by the NHM (red circles with the vertical line) and the atmosphere-wave-ocean coupled model (light blue circles with the vertical line) and simulated central pressures with atmospheric initial conditions at 12 UTC on 25 July, 06, 12, 18 UTC on 27 July and 00 UTC on 28 July. See Table 1 for the identity of the different simulations. (b) Time series showing ensemble mean radius of the maximum winds at 20-m height with the error bar (one standard deviation) simulated by the NHM (red circles with the vertical line) and CPL (light blue circles with the vertical line).

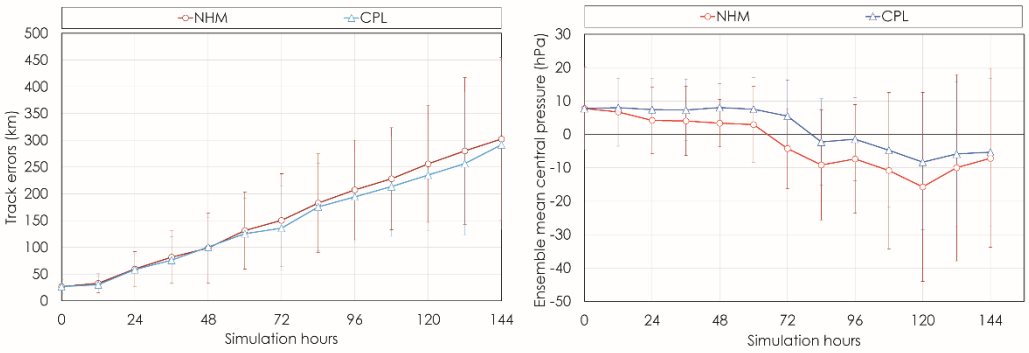

Fig.6 (Left) Mean track errors with respect to the best track position and (right) central pressure errors with respect to the mean best track central pressure in the noncoupled-model simulations (red circles and lines) and coupled-model simulations (blue circles and lines). The error bars indicate one standard deviation.

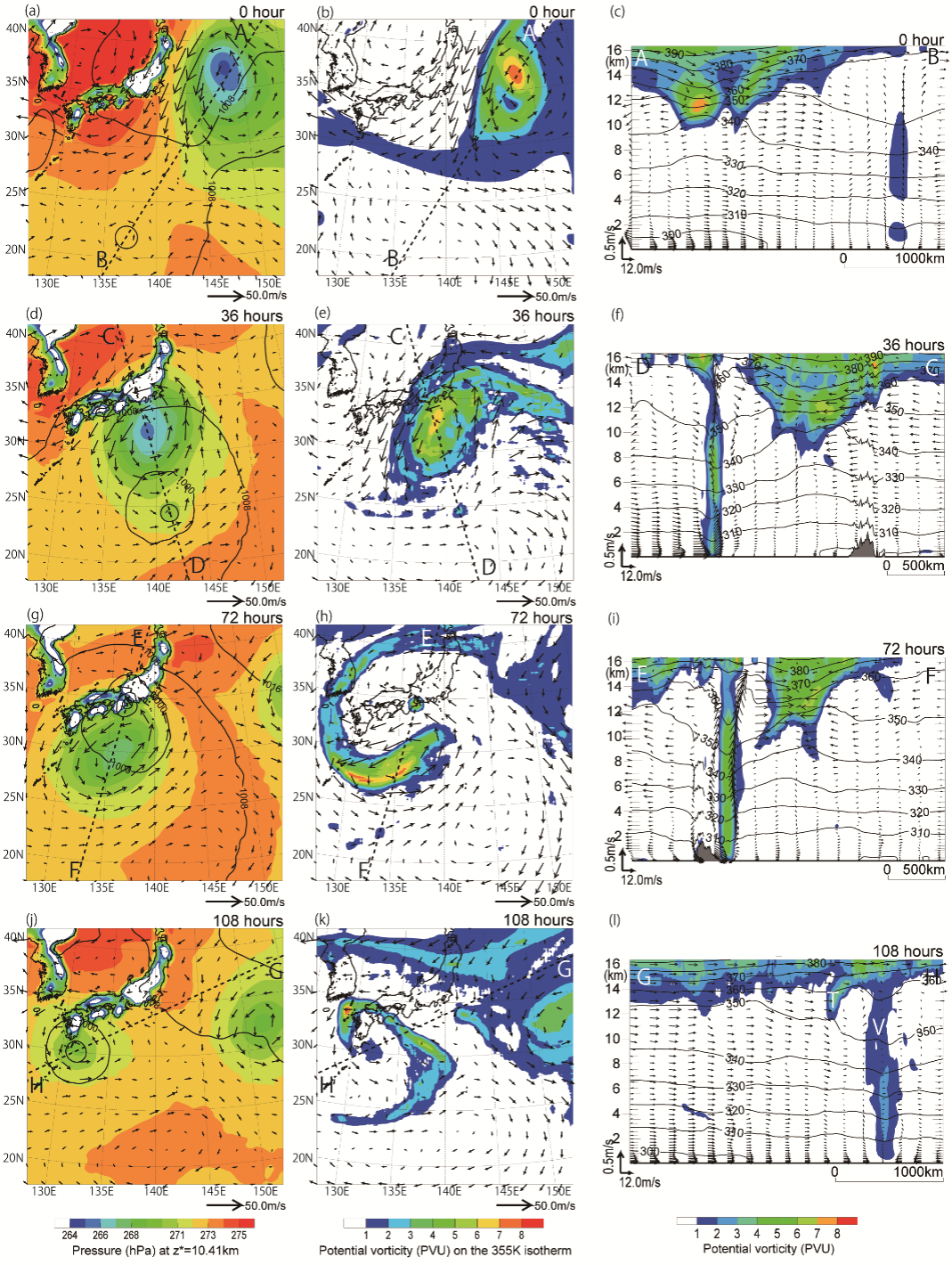

Fig.7 Simulations by the NHM with initial conditions at 12 UTC on 25 July at integration times of (a–c) 0 h, (d–f) 36 h, (g–i) 72 h, and (j–l) 108 h. Left panels show the distribution of pressure at approximately 10 km altitude (colors), sea-level pressure (black lines, contour interval 8 hPa), and wind vectors at approximately 10 km altitude. Center panels show the distribution of PV (colors) and wind vectors on the 355 K isotherm. Right panels show a vertical profile of PV (colors), potential temperature (black lines, interval 10 K), and

horizontal-vertical wind vectors parallel to the cross section along the line between the centers of Jongdari and the UTCL (see section 3.2), shown as dashed lines in the left and center panels. "A-H" indicate the location of the start and end points of the cross section. ‘T’ and ‘V’ in Fig. 7l are explained in the text.

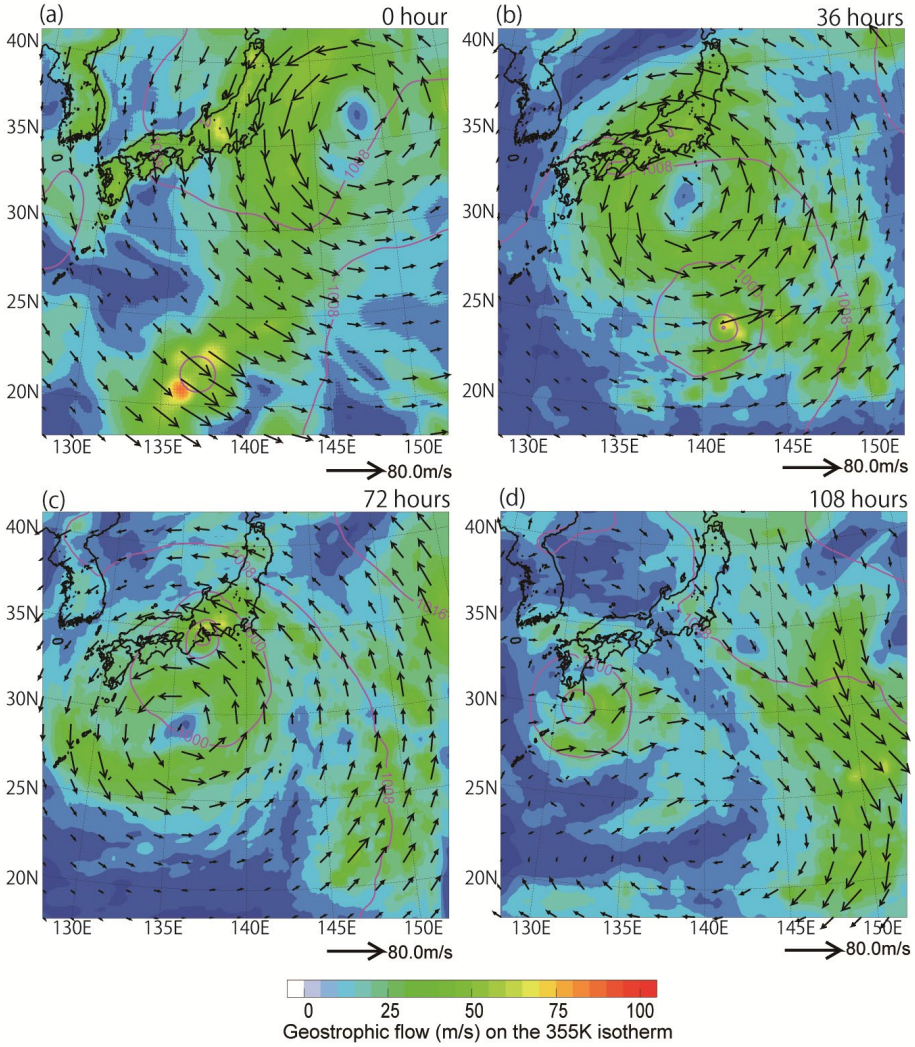

Fig. 8 Horizontal distribution of the magnitude of geostrophic flow on the 355 K isotherm (colors), sea-level pressure (purple lines, contour interval 8 hPa), and geostrophic flow vectors on the 355 K isotherm simulated by the NHM with initial conditions at 12 UTC on 25 July at integration times of (a) 0 h, (b) 36 h, (c) 72 h, and (d) 108 h.

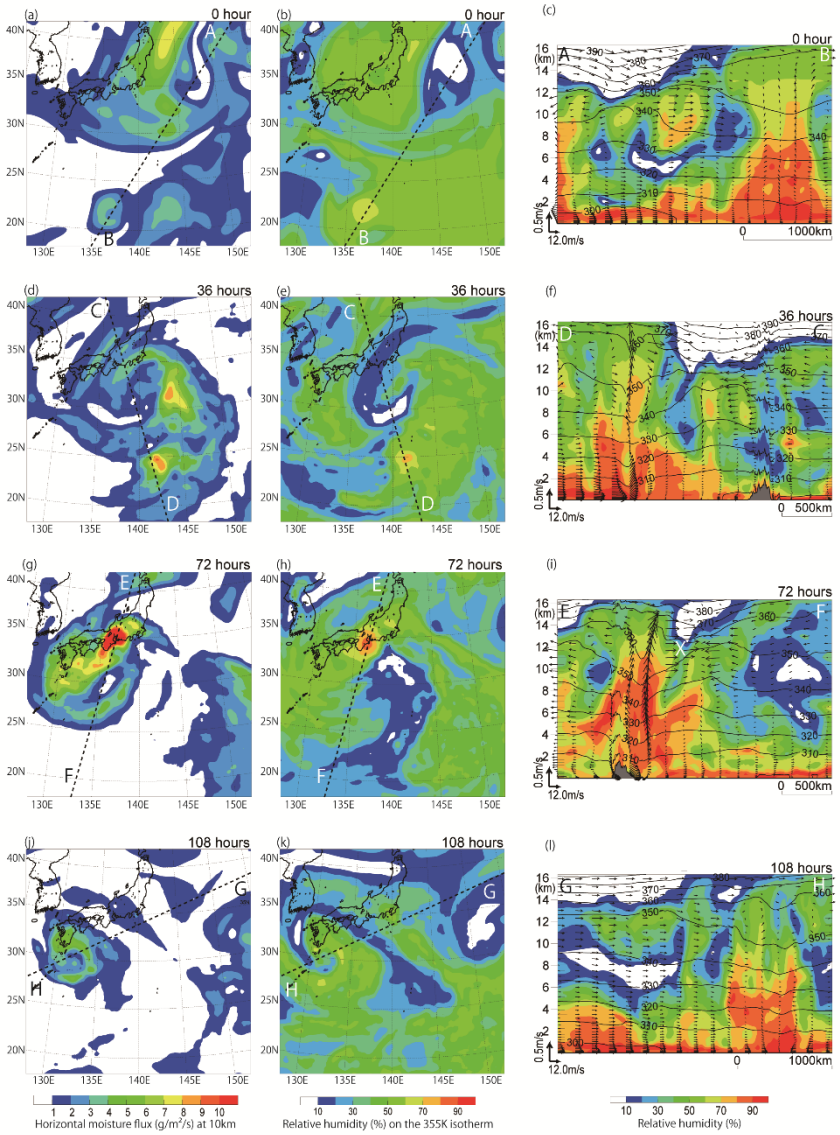

Fig.9 Simulations by the NHM with initial conditions at 12 UTC on 25 July at integration times of (a–c) 0 h, (d–f) 36 h, (g–i) 72 h, and (j–l) 108 h. Left panels show the distributions of horizontal moisture flux (colors) at approximately 10 km altitude. Center panels show relative humidity on the 355 K isotherm (colors). Right panels show a vertical profile of relative humidity (colors), potential temperature (black lines, interval 10 K), and horizontal-vertical wind vectors parallel to the cross section along the line between the centers of Jongdari and the UTCL shown as white lines in the left and center panels. "A-H" indicate the location of the start and end points of the cross section. 'X' in Fig. 9i is explained in the text.

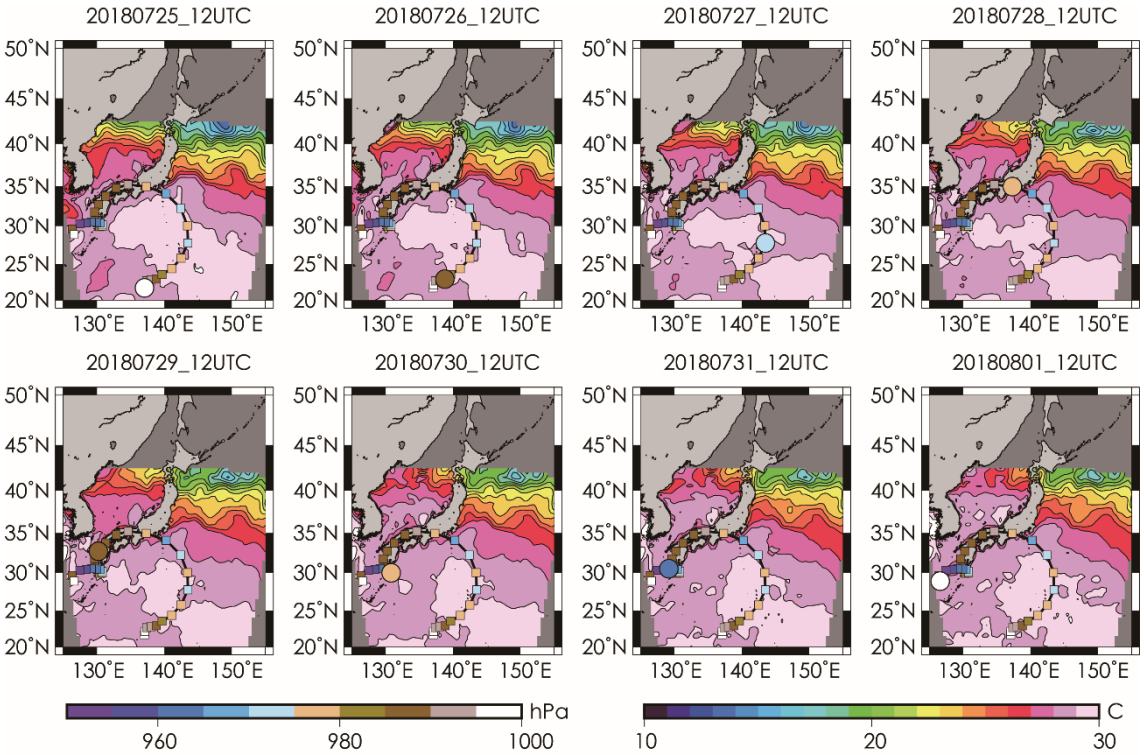

Fig.10 Horizontal distribution of SST simulated by the CPL from 25 July to 1 August with initial conditions at 12 UTC on 25 July and simulated positions of Jongdari every 6 h (circles). The large circle indicates the simulated position of Jongdari at the time of the plot. Colors of the circles indicate the simulated central pressure.

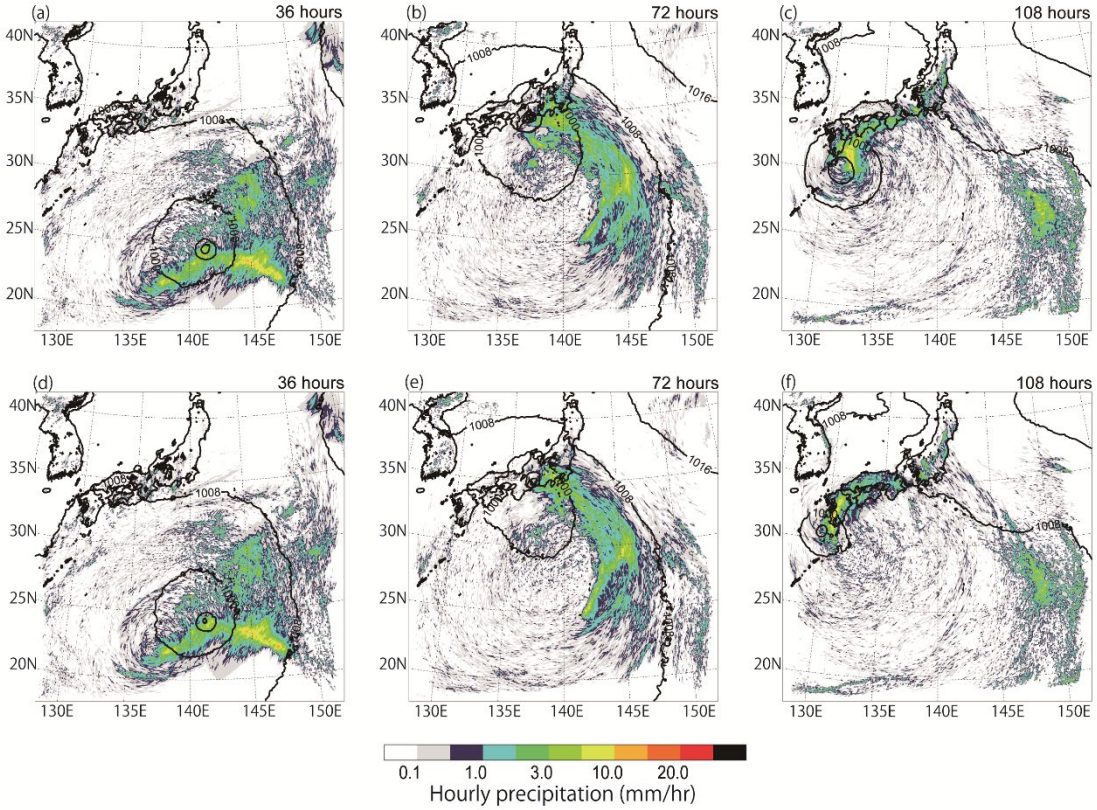

Fig.11 Distributions of hourly precipitation (colors) and sea-level pressure (contours, interval 8 hPa) in the noncoupled-model simulation at integration times of (a) 36 h, (b) 72 h, and (c) 108 h and in the coupled-model simulation at integration times of (d) 36 h, (e) 72 h, and (f) 108 h.

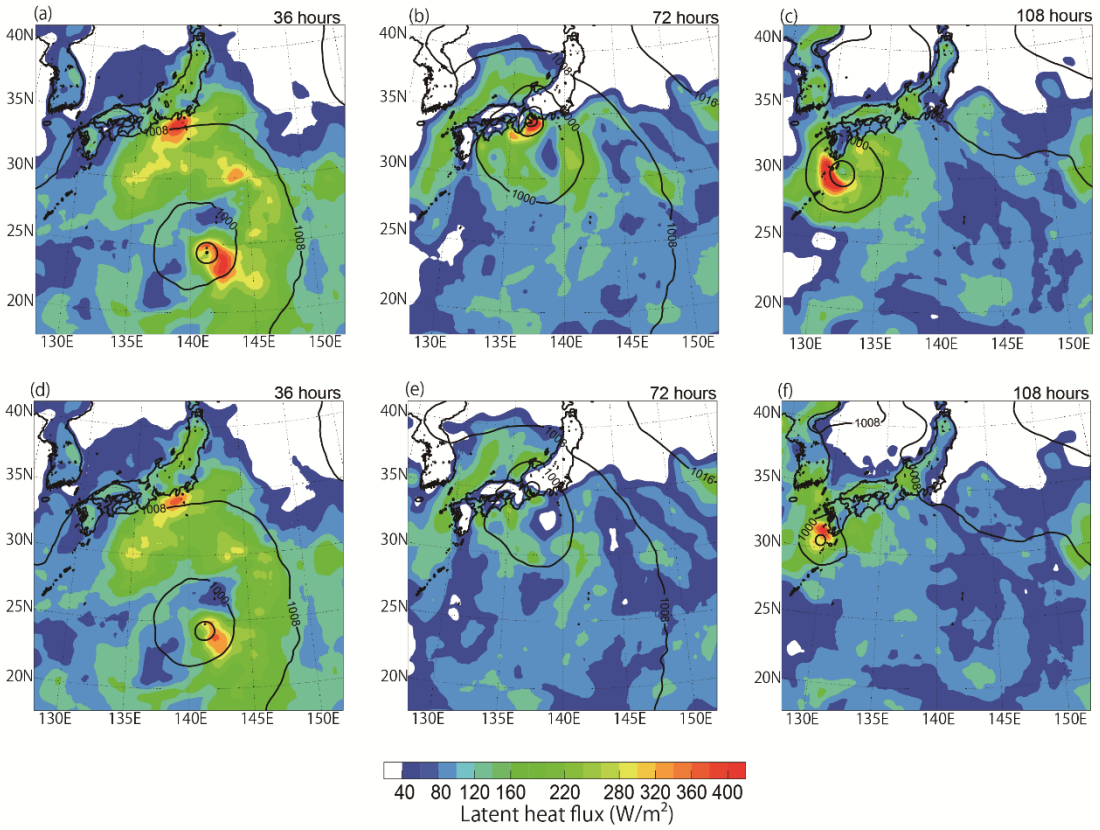

Fig.12 Distributions of latent heat flux (colors) and sea-level pressure (contours, interval 8 hPa) in the noncoupled-model simulation at integration times of (a) 36 h, (b) 72 h, and (c) 108 h and in the coupled-model simulation at integration times of (d) 36 h, (e) 72 h, and (f) 108 h.

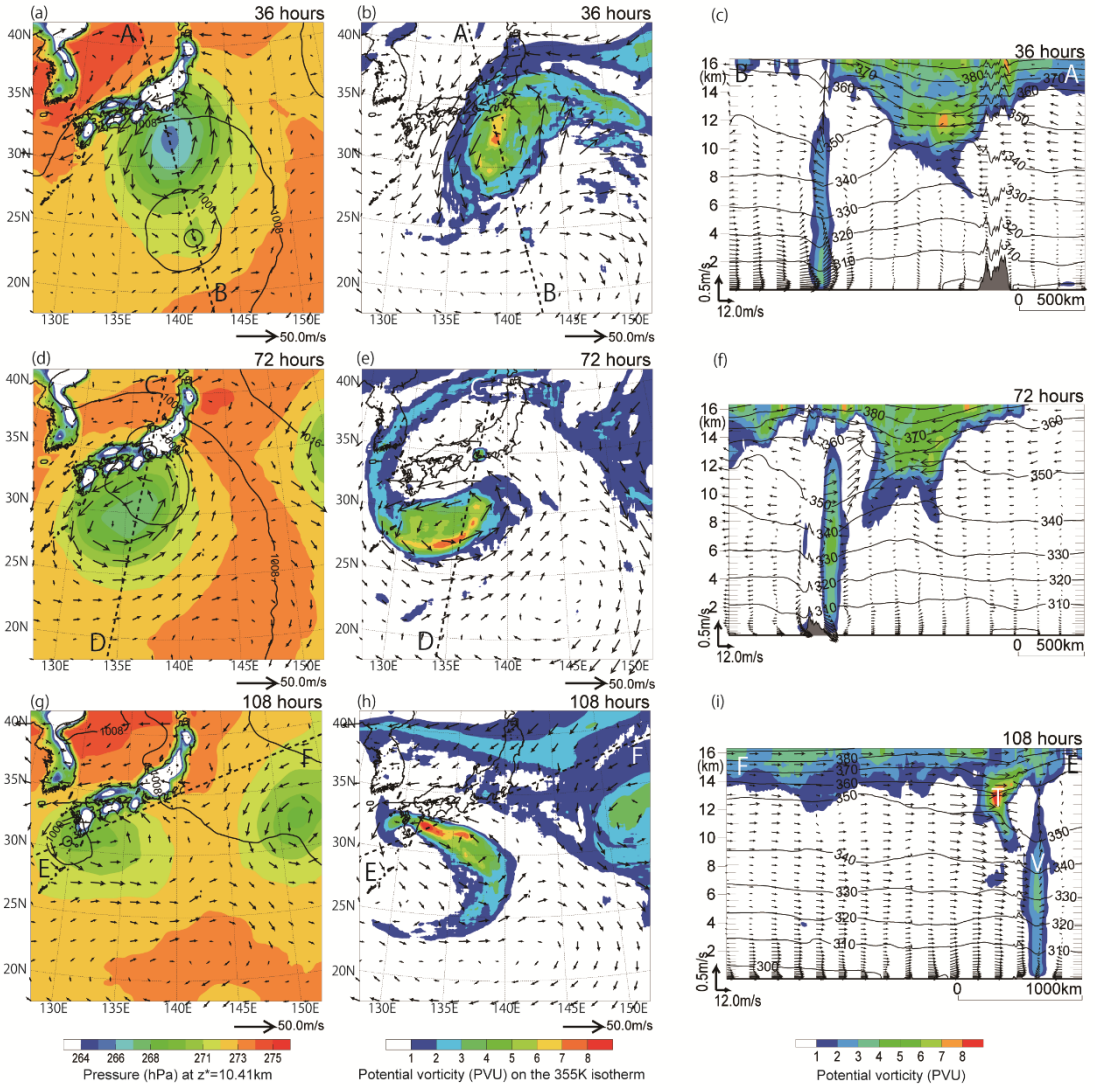

Fig.13 Simulations by the CPL with initial conditions at 12 UTC on 25 July at integration times of (a–c) 36 h, (d–f) 72 h, and (g–i) 108 h, corresponding to the noncoupled-model simulation in Fig. 7. Symbols and colors are the same as Fig. 7. 'T' and 'V' in Fig. 13i are explained in the text.

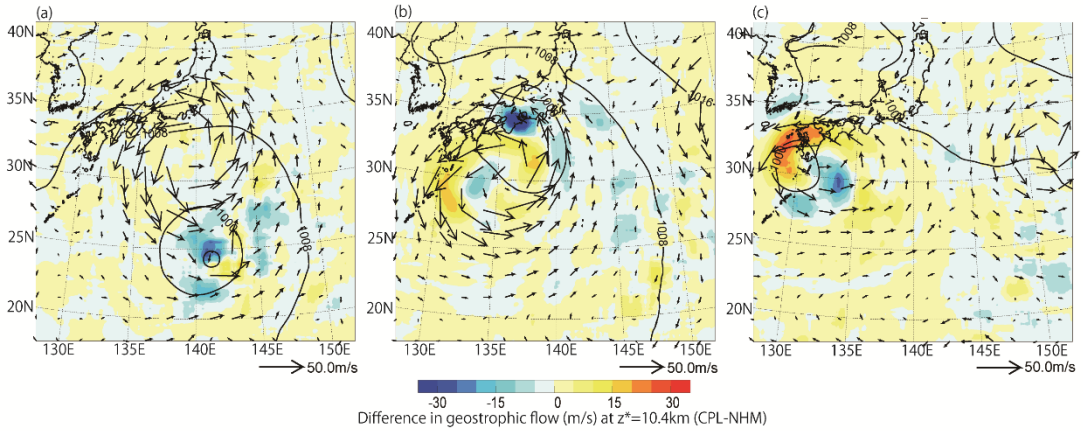

Fig.14 Horizontal distributions in the difference in magnitude (colors) and vector (arrows) of geostrophic flows between the noncoupled-model simulations and the coupled-model simulations (CPL minus NHM) with initial conditions at 12 UTC on 25 July at integration times of (a) 36 h, (b) 72 h, and (c) 108 h. The contours indicate sea-level pressure simulated by the CPL. The interval is 8 hPa.

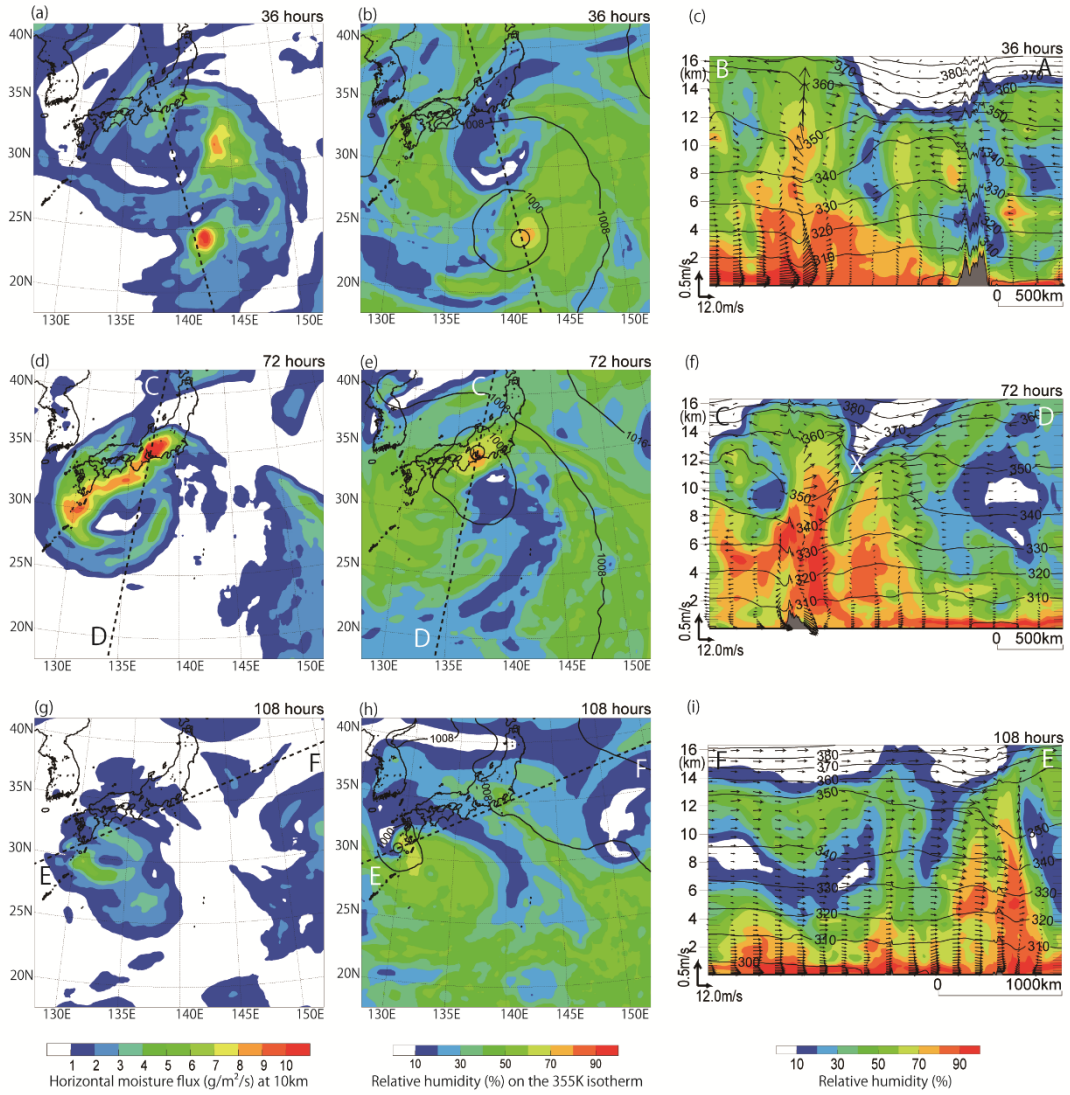

Fig.15 Simulations by the CPL with initial conditions at 12 UTC on 25 July at integration times of (a–c) 36 h, (d–f) 72 h, and (g–i) 108 h, corresponding to the noncoupled-model simulation in Fig. 9. Symbols and colors are the same as Fig. 9. 'X' in Fig. 15f is explained in the text.

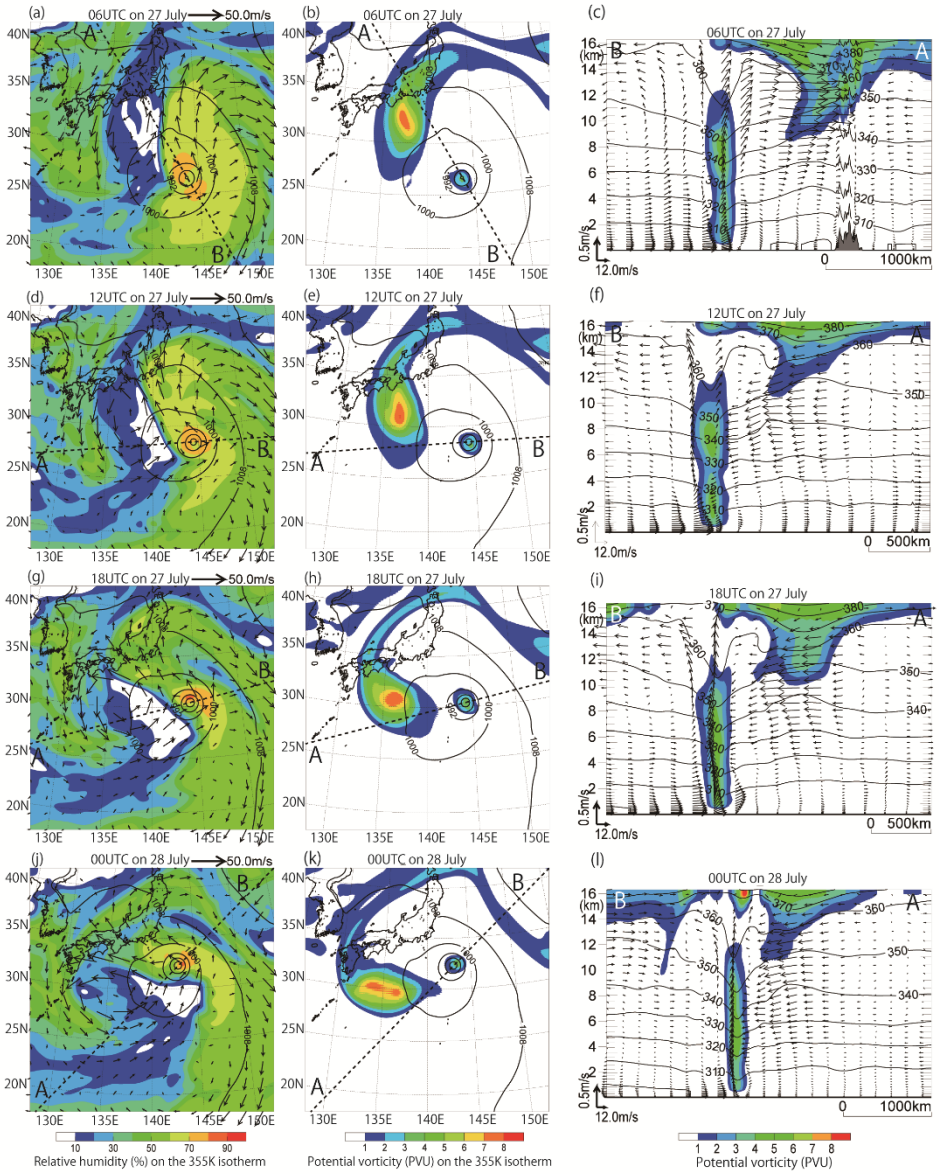

Fig.16 Atmospheric conditions based on JMA data at four different times: (a–c) 06 UTC on 27 July, (d–f) 12 UTC on 27 July, (g–i) 18 UTC on 27 July, and (j–l) 00 UTC on 28 July. These were used as initial conditions for simulations ending at 00 UTC on 30 July (see text). Left panels show the distribution of relative humidity on the 355 K isotherm (colors), wind vectors at that altitude, and sea-level pressure (black lines, contour interval 8 hPa). Center panels show the distribution of PV (colors) and sea-level pressure (black lines, contour interval 8 hPa). Right panels show a vertical profile of PV (colors), potential temperature (black lines, interval 10 K), and horizontal-vertical wind vectors parallel to the cross section along the line between the centers of Jongdari and the UTCL (see section 3.2), shown as dashed lines in the left and center panels. "A-H" indicate the location of the start and end points of the cross section.

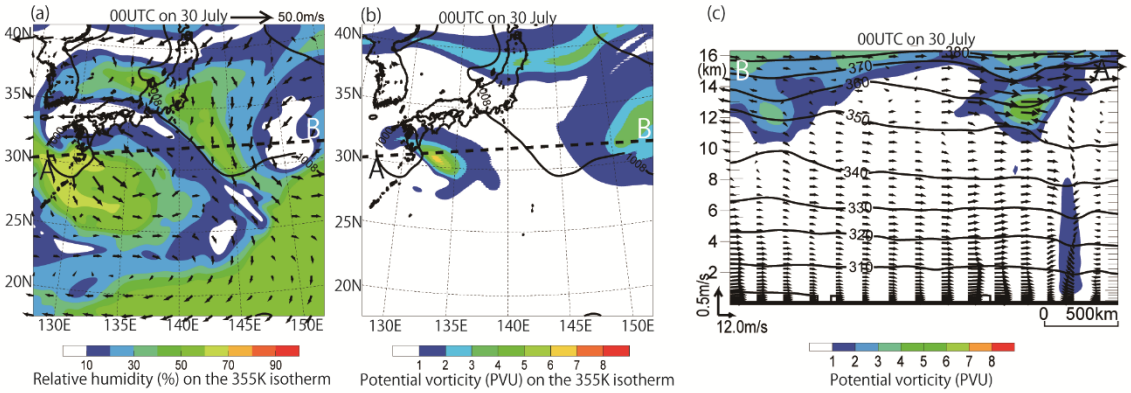

Fig.17 Atmospheric conditions based on JMA 6-hourly global atmospheric analysis data at 00 UTC on 30 July. (a) The distribution of relative humidity on the 355 K isotherm (colors), wind vectors at that altitude, and sea-level pressure (purple lines, contour interval 8 hPa). (b) The distribution of PV (colors) and sea-level pressure (black lines, contour interval 8 hPa). (c) A vertical profile of PV (colors), potential temperature (black lines, interval 10 K), and horizontal-vertical wind vectors parallel to the cross section along the line between the centers of Jongdari and the UTCL (see section 3.2), shown as dashed lines in the left and center panels.

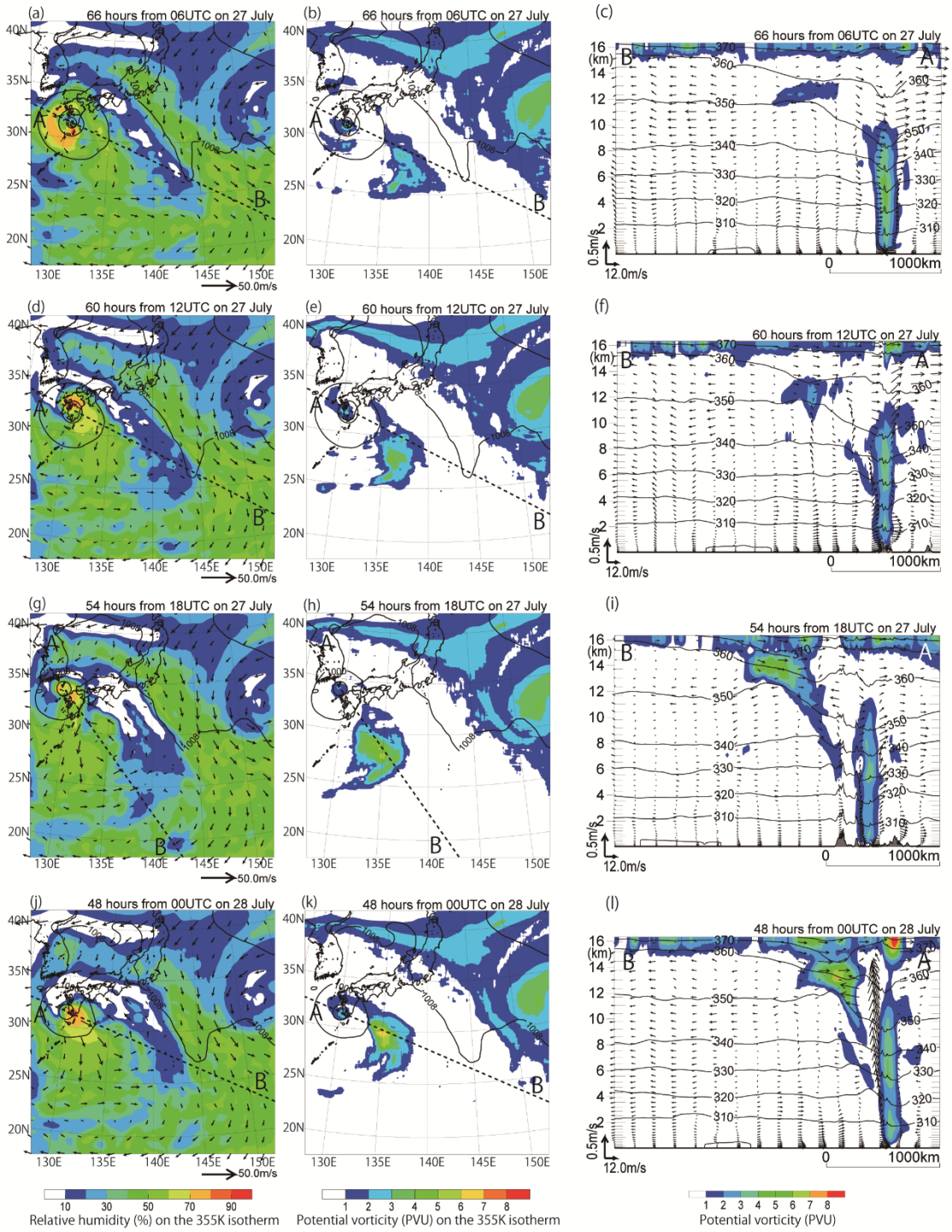

Fig.18 Results of simulations by the NHM at 00 UTC on 30 July from the initial conditions in Fig. 16.

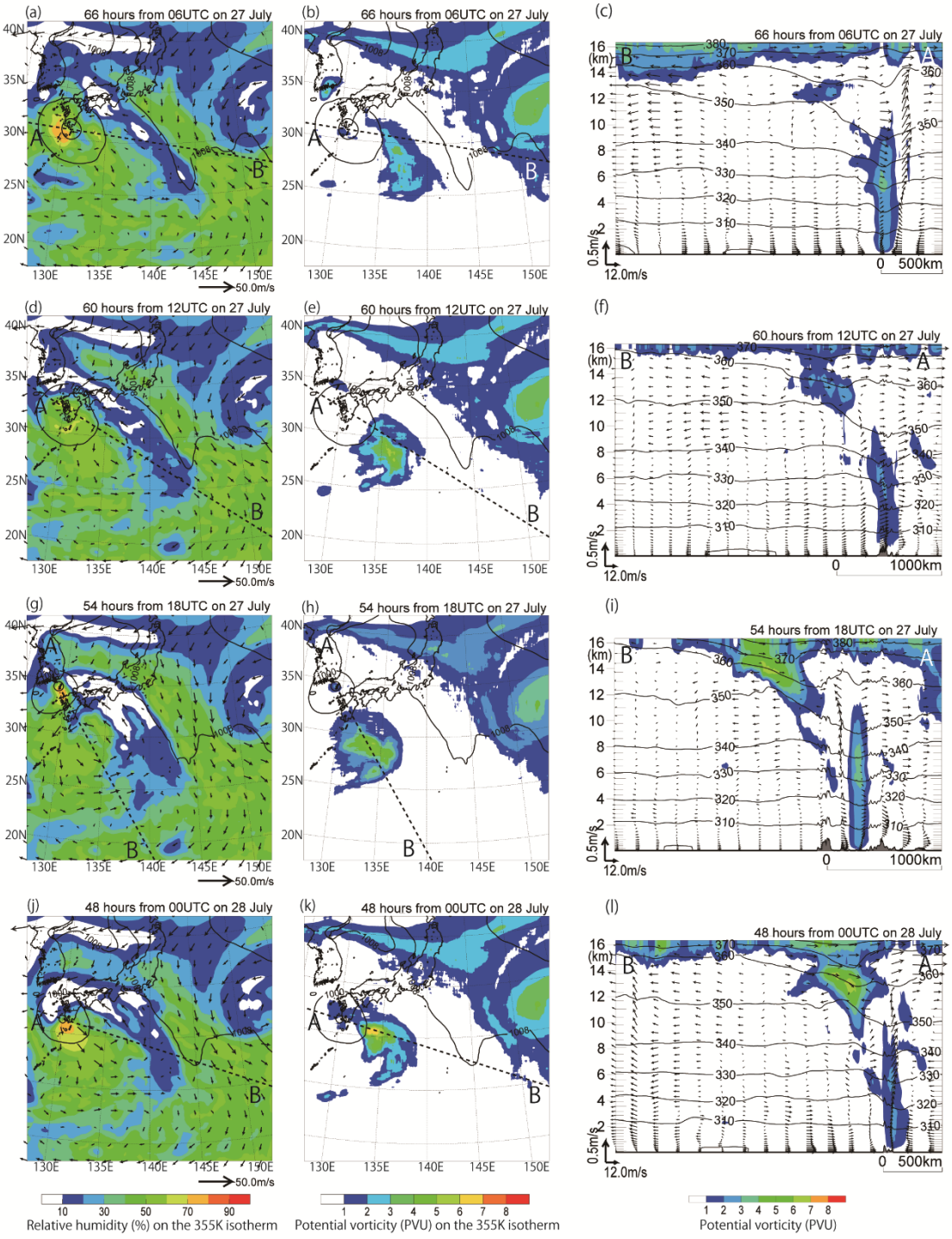

Fig.19 Results of simulations by the CPL at 00 UTC on 30 July from the initial conditions in Fig. 16.

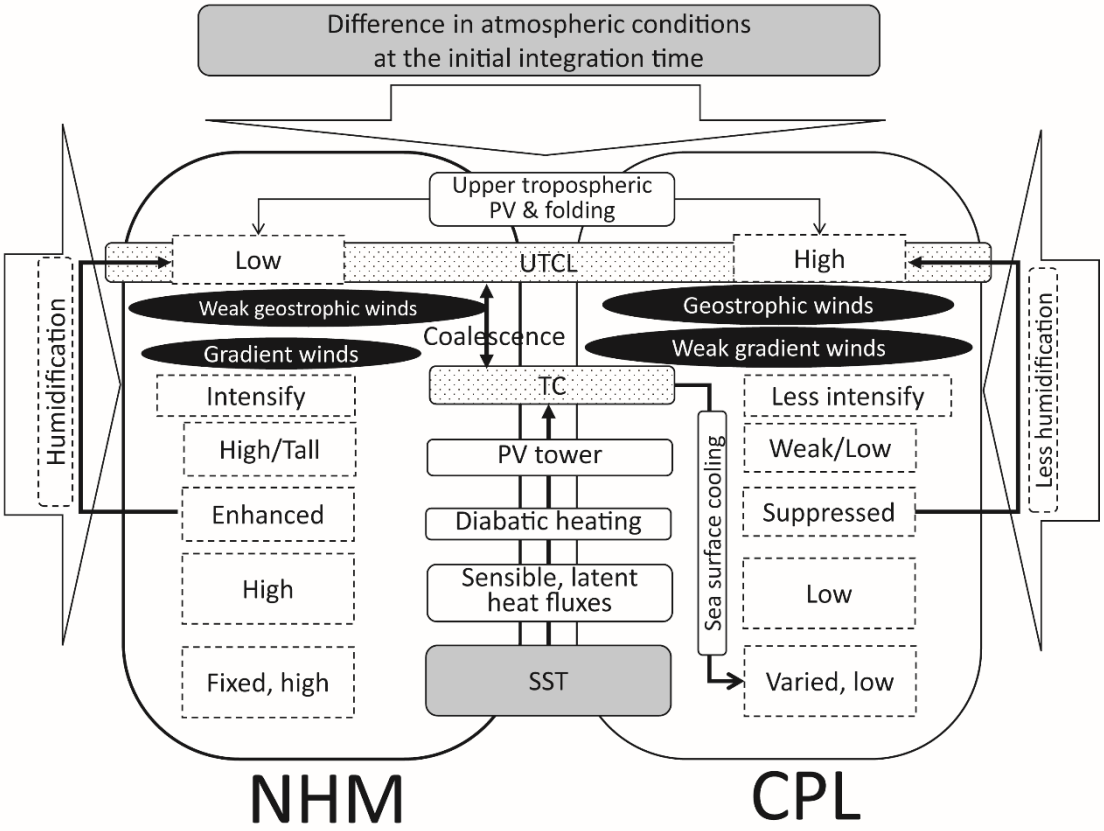

Fig.20 Schematic diagrams depicting the interactions between Jongdari and the UTCL (hatched solid boxes) addressed in this study. Factors associated with uncertainty of atmospheric environments and ocean coupling are shown. Solid boxes shows factors addressed in this study. SST and difference in atmospheric initial conditions are shaded. Solid ellipses indicate the comparison of geostrophic and gradient winds that affect simulated TC tracks between the noncoupled- and coupled-model simulations. Dashed boxes show the comparison regarding the factor in each solid box. Humidification indicated in large arrows is directly affected by diabatic heating and the effect is accumulated in the atmospheric environments, resulting in the impact on UTCL. Difference in atmospheric environments at the initial time indicated in another large arrow is also one of the atmospheric environment factors that affects the simulations of TC and UTCL.